NASA TECHNICAL NOTE

NASA TN D-7835

WEAK INCIDENT SHOCK INTERACTIONS WITH MACH 8 LAMINAR BOUNDARY LAYERS
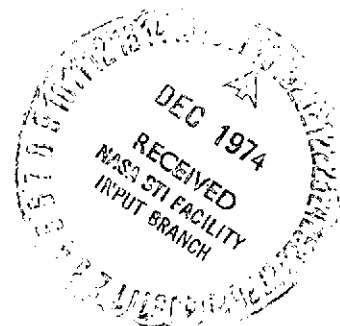
by Louis G. Kaufman II and Charles B. Johnson

Langley Research Center
Hampton, Va. 23665

NATIONAL AERONAUTICS AND SPACE ADMINISTRATION • WASHINGTON, D. C. • DECEMBER 1974

1. Report No. NASA TN D-7835	2. Government Accession No.	3. Recipient's Catalog No.
4. Title and Subtitle WEAK INCIDENT SHOCK INTERACTIONS WITH MACH 8 LAMINAR BOUNDARY LAYERS		5. Report Date December 1974
		6. Performing Organization Code
7. Author(s) Louis G. Kaufman II and Charles B. Johnson		8. Performing Organization Report No. L-9792
9. Performing Organization Name and Address NASA Langley Research Center Hampton, Va. 23665		10. Work Unit No. 505-11-31-02
		11. Contract or Grant No.
12. Sponsoring Agency Name and Address National Aeronautics and Space Administration Washington, D.C. 20546		13. Type of Report and Period Covered Technical Note
		14. Sponsoring Agency Code

15. Supplementary Notes

Louis G. Kaufman II is employed in the Research Department, Grumman Aerospace Corporation; work performed as a Langley-Industry Research Associate.

16. Abstract

Weak shock-wave interactions with boundary layers on a flat plate were investigated experimentally in the Langley Mach 8 variable-density tunnel for plate-length Reynolds numbers ranging from 0.46×10^6 to 2.5×10^6. The undisturbed boundary layers were laminar over the entire plate length. Pressure and heat-transfer distributions were obtained for wedge-generated incident shock waves that resulted in pressure rises ranging from 1.36 to 4.46 (both nonseparated and separated boundary-layer flows). The resulting heat-transfer amplifications ranged from 1.45 to 14. The distributions followed established trends for nonseparated flows, for incipient separation, and for laminar free-interaction pressure rises. The experimental results corroborated established trends for the extent of the pressure rise and for certain peak heat-transfer correlations. Because of the many factors that strongly affect laminar boundary layers, and because transition frequently occurred prior to the end of the interaction region, the data did not support the simpler correlations of peak heating with peak pressure that have been proposed previously.

17. Key Words (Suggested by Author(s)) Viscid-inviscid interaction Laminar-transitional boundary layer Separation	18. Distribution Statement Unclassified – Unlimited STAR Category 12		
19. Security Classif. (of this report) Unclassified	20. Security Classif. (of this page) Unclassified	21. No. of Pages 45	22. Price* $3.75

WEAK INCIDENT SHOCK INTERACTIONS WITH

MACH 8 LAMINAR BOUNDARY LAYERS

By Louis G. Kaufman II[1] and Charles B. Johnson
Langley Research Center

SUMMARY

Weak shock-wave interactions with boundary layers on a flat plate were investigated experimentally in the Langley Mach 8 variable-density tunnel for plate-length Reynolds numbers ranging from 0.46×10^6 to 2.5×10^6. The undisturbed boundary layers were laminar over the entire plate length. Pressure and heat-transfer distributions were obtained for wedge-generated incident shock waves that resulted in pressure rises ranging from 1.36 to 4.46 (both nonseparated and separated boundary-layer flows). The resulting heat-transfer amplifications ranged from 1.45 to 14. The distributions followed established trends for nonseparated flows, for incipient separation, and for laminar free-interaction pressure rises. The experimental results corroborated established trends for the extent of the pressure rise and for certain peak heat-transfer correlations. Because of the many factors that strongly affect laminar boundary layers, and because transition frequently occurred prior to the end of the interaction region, the data did not support the simpler correlations of peak heating with peak pressure that have been proposed previously.

INTRODUCTION

Shock waves that impinge on a surface can greatly amplify the local heat transfer and pressure loads on the surface. The adverse pressure gradient associated with a sufficiently strong shock wave causes a laminar boundary layer to separate from the surface. Although the problem is well recognized and has received much attention (refs. 1 to 4), there are still no adequate simple methods for predicting pertinent geometric features of the separation region and the increased heating at reattachment.

In general, when boundary-layer separation occurs because of shock interaction, there is a region of reverse flow (fig. 1) that terminates where the separated boundary layer reattaches to the surface, with attendant high pressures and heating rates. The compression waves emanating from the separation location coalesce into a shock, and

---

[1] Research Department, Grumman Aerospace Corporation; work performed as a Langley-Industry Research Associate.

the pressure rises to a "plateau" value. For laminar boundary layers, the heating rate drops below the undisturbed value at the onset of separation. Immediately downstream of the compression waves are expansion waves that emanate from the top of the separation bubble. Downstream of the expansion waves there are recompression waves (coalescing into a shock) that occur with reattachment of the separated flow, and the pressures and heating rates can attain very large values. Therefore, obtaining meaningful experimental pressure and heat-transfer data in a shock—laminar-boundary-layer interaction region involves careful design of experimental tests and model. For example, in the present tests to minimize extraneous effects, a simple two-dimensional configuration was chosen: wedge-generated shock waves interacting with boundary layers on a sharp-leading-edge flat plate. The wedges were designed to provide as long a region (streamwise) of constant pressure as possible in the given wind tunnel. As sketched in figure 1, the wedges were positioned as far forward as possible. The wedge trailing edge was positioned near the plate bow wave to minimize reflected waves. The experiments were conducted in the Langley Mach 8 variable-density tunnel for plate length Reynolds numbers ranging from 0.46×10^6 to 2.5×10^6.

The experiments provided pressure and heating-rate distributions for incident shock interactions with initially laminar boundary layers, and schlieren photographs of the interaction flow field. Many investigators (refs. 5 to 11) examined the peak heating at reattachment and several proposed simple correlations in the form $h_{pk} \propto (P_{pk})^n$ (peak heating proportional to the peak pressure raised to a power n). However, the values of the exponent n in these current correlations vary from 0.5 to 1.3, an unacceptable difference. An objective of the subject work was to reexamine these correlations in an attempt to resolve their discrepancies. In addition to this objective, the present data are compared with existing, simple, analytical methods for predicting "free interaction" pressure rises (refs. 12 and 13), plateau pressure levels (refs. 2 and 14 to 16), criteria for incipient separation (refs. 17 to 21), and the extent of laminar separation (refs. 21 to 25).

SYMBOLS

c	specific heat of model material, J/kg-K
c_f	coefficient of friction of boundary layer
c_p	specific heat of air flow, J/kg-K
F(s)	similarity function for free-interaction pressure rise (see eq. (6))
H	ratio of disturbed to undisturbed heat-transfer coefficients at same location

2

h	heat-transfer coefficient, W/m^2K
ℓ	length of pressure rise upstream of x_i
M	Mach number
N_{Pr}	Prandtl number
N_{St}	Stanton number, $\equiv h/(\rho c_p V)_1$
n	exponent in correlations of peak heating with peak pressure
P	ratio of disturbed to undisturbed pressure ratios, $\dfrac{(p/p_t)_{disturbed}}{(p/p_t)_{undisturbed}}$
p	pressure, N/m^2
$\dot{q}$	heating rate, W/m^2
R	Reynolds number based on free-stream conditions and a unit length of 1 meter
$R_{x,i}$	Reynolds number based on local undisturbed flow conditions and length x_i
r	recovery factor
$s \equiv (x - x_o)/(x_f - x_o)$	
T	temperature, K
t	time, sec
V	velocity, m/sec
x	streamwise distance measured from flat-plate leading edge, m
x_f	reference location used for free-interaction pressure rise similarity function F, $x = x_f$ at $F = 0.81$
α	turning angle for incipient separation, radians
γ	ratio of specific heats (taken as 1.4 herein)

Δp uncertainty in measured pressure, N/m^2

$\Delta \nu$ change in Prandtl-Meyer angle for isentropic compression, deg

δ boundary-layer thickness, m

θ angle of attack of wedge shock generator, deg

λ proportionality constant in equation (8), $\lambda(T_w/T_t)$

μ viscosity, $N\text{-}sec/m^2$

ρ density, kg/m^3

τ thin-wall thickness, m

ϕ flow-deflection angle at reattachment

Subscripts:

aw   adiabatic wall conditions

e   conditions at outer edge of boundary layer

i   incident shock location on plate surface in absence of boundary layer

incip   conditions for incipient separation of laminar boundary layer

m   model material (stainless steel)

plat   plateau value

pk   peak (maximum) value

sep   local conditions at separation location

sl   shear layer

t   total (stagnation) conditions

w   wall conditions

o   local undisturbed flow conditions at location where interaction pressure starts to rise

1   local undisturbed flow conditions

2   conditions immediately downstream of incident shock

3   conditions downstream of reflected incident shock

∞ free-stream conditions

A comma is used to indicate a double subscript. For example, $H_{P,pk}$ refers to the value of H at P_{pk}.

APPARATUS AND TEST PROCEDURES

Model Design

The model configurations and tunnel flow conditions were chosen to provide data for shock-wave boundary-layer interactions with a minimum of extraneous effects. A simple two-dimensional configuration was chosen: wedge-generated shock waves impinging on a flat-plate surface. The wedge and plate were designed to keep extraneous waves (such as those from the wedge trailing edge) as far away from the interaction region as possible. (See fig. 1.) Small wedge angles were used to insure obtaining small interaction flow regions and primarily to insure obtaining fully reattached flow ahead of the influence of any extraneous effects. Tunnel flow conditions were chosen to yield laminar-boundary-layer flow over the entire flat-plate surface in the absence of an incident shock wave.

Photographs of the model (fig. 2) show the wedge shock generator sting mounted to a vertical strut. The instrumented flat-plate shock receiver is cantilevered forward from the same strut. The wedge has a span of 15.25 cm; the flat plate has a span of 17.46 cm. The chords of the wedge and flat plate are indicated in the profile view sketched in figure 3. The instrumented center line of the flat plate is well within the region bounded by the tip Mach cones.

The wedge shock generator could be set at various streamwise stations and at various heights above the flat-plate shock receiver. In order to avoid reflections of the plate bow wave from the wedge surface, the wedge trailing edge is positioned just above the calculated position of the bow wave from the plate leading edge. (See fig. 1.) Indeed, it

was hoped that this bow wave would partially cancel the expansion fan emanating from the wedge trailing edge.

The wedge shock generator can be set at any one of three incidence angles with respect to the free-stream flow: $\theta = 1^O$, 3°, or 5°. The effective wedge angles are somewhat different for two reasons. The displacement thickness growth of the boundary layer on the wedge surface increases the effective wedge angle, whereas the interaction with the plate bow wave decreases the effective wedge angle. The maximum static-pressure rise on the plate surface is that associated with the shock caused by the effective wedge angle as well as its reflection from the flat-plate surface. If these considerations are taken into account, the chosen angles are sufficient to provide data for unseparated flows as well as for small regions of separated flow. (See refs. 19 to 21.) Larger angles would cause extensive regions of separated flow and increase the probability of the free shear layer becoming transitional prior to reattachment (ref. 26) and/or the reattachment region being influenced by the wave from the wedge trailing edge. Thus, the shock generator is designed to yield as large a region of "clean" shock impingement interaction flow as possible.

There are two (interchangeable) flat-plate shock receivers. Both have machined sharp leading edges. One is instrumented with 48 pressure orifices evenly spaced along the plate center line; and one, with thermocouples at the same locations. (See fig. 3.) The first instrumentation location is 13.94 cm downstream of the leading edge; the pressure orifices and thermocouples are evenly spaced 0.508 cm apart. The iron-constantan thermocouples are spot welded to the inner surface of a "thin skin" section of the plate used for heat-transfer measurements. The skin thickness in this region is 0.076 cm. The pressure instrumented plate has a constant thickness of 0.318 cm.

Test Conditions

The experiments were conducted in the Langley Mach 8 variable density tunnel. This is a blowdown wind tunnel with a closed circular test section, with a diameter of 45.72 cm, that can provide Mach 8 free-stream flows for unit Reynolds numbers R varying from 0.60×10^6 to 30×10^6 per meter. (See refs. 27 and 28.) The tunnel has a model injection system directly beneath the test section. Although full injection to tunnel center line requires approximately 0.8 second, the model passes through the tunnel wall shear layer in just 0.2 second. Therefore, the model experiences nonuniform flow heating for just 0.2 second. A 12.5-m-diameter sphere and an 18.3-m-diameter sphere were used in conjunction to provide a vacuum system with sufficient capacity to enable the low pressure measurements to stabilize within the tunnel running time (approximately 4 minutes).

The experiments were conducted at four tunnel stagnation pressure p_t levels. They are listed in table I along with the values of the total temperatures T_t. The calibrated free-stream Mach numbers M_∞ corresponding to these (relatively low) tunnel pressure levels are listed (ref. 27) as well as the values of the free-stream unit Reynolds numbers per meter. Pressure, heat transfer, and schlieren flow photographic data were obtained for all model configurations ($\theta = 1^\circ$, 3°, and 5°).

TABLE I.- TUNNEL FLOW CONDITIONS

p_t		T_t, K	M_∞	R/m
MN/m^2	psia			
0.48	70	710	7.68	1.3×10^6
.71	103	710	7.73	1.9
1.51	219	730	7.80	3.7
2.96	429	770	7.87	6.5

Test Procedures and Data Reduction

For the pressure and heat-transfer experiments, the tunnel flow was first started and established, the model was injected into the tunnel flow, data were recorded, and then the model was retracted prior to stopping the tunnel flow. Pressures were measured by using 39 multirange capacitance-type transducers and 9 single-range strain-gage transducers. Heat-transfer data were obtained by using thermocouples and the thin-wall transient-temperature technique. Schlieren flow photographs were taken during each pressure and heat-transfer tunnel run. Additional tunnel runs were made to obtain schlieren flow photographs with the model mounted further forward in the test section. The model wall temperature T_w was measured and recorded after each pressure run was completed.

Although 80 percent of the pressure orifices are connected to multirange capacitance-type transducers, which are much more accurate than the single-range strain-gage transducers, the accuracy of the pressure gages is considered herein to be that of the strain-gage transducers; that is, $\Delta p = \pm 8.6$ N/m^2 (0.00125 psi). The resulting uncertainties in terms of free-stream static pressures vary from $\pm 0.13 p_\infty$ for the lowest pressure runs to $\pm 0.03 p_\infty$ for the highest pressure runs.[2]

The temperature time history of each thermocouple is recorded at the rate of 40 readings/second on magnetic tape by an analog-digital data-recording system. These time histories are used to obtain the temperature rise rates $\left(dT_w/dt\right)$, and these rates are

---

[2] This is the calibrated accuracy of the pressure instrumentation. The scatter in the pressure data, as evidenced in the following section, is considerably larger.

used to obtain the heating rates $\dot{q}_w$ from

$$\dot{q}_w = \rho_m c_m \tau_m \frac{dT_w}{dt} \tag{1}$$

where ρ_m and c_m are the density and specific heat of the model material (stainless steel), and τ_m is the thickness of the thin wall (0.076 cm).

Once the model starts to experience heating, the error due to conduction of heat along the model surface increases with time, whereas the aerodynamic heating rate decreases with time. Thus, the percent of heating due to conduction relative to the indicated aerodynamic heating increases rapidly with time. Therefore, the data must be reduced as early as possible after aerodynamic heating starts.

For these experiments, the temperature-time derivative in equation (1) is obtained by least-squares fitting a linear temperature-time variation to the temperatures recorded during the interval from 0.1 to 1.1 seconds after the model reaches the tunnel center line. The simple linear variation is best suited for reducing the scatter in the relatively low heating-rate data. The scatter results from the electronic "noise" in the data recording system. The short time intervals and the relatively low heating rates lead to small variations in wall temperature along the model surface, and negligible conduction effects.

The experimental heat-transfer coefficient h is calculated from

$$h = \frac{\dot{q}_w}{T_{aw} - T_w} \tag{2}$$

where

$$T_{aw} = T_\infty + r\left(T_t - T_\infty\right) \tag{3}$$

The laminar boundary-layer recovery factor $\left(r \approx \sqrt{N_{Pr}} \approx 0.85\right)$ is used to calculate the adiabatic wall temperature T_{aw} for the reduction of all the heating data herein.

The heat-transfer data are obtained during the initial heating of the model while the wall is relatively cool $\left(T_w \approx 0.4T_t\right)$. The longer run times required for the pressure readings to stabilize result in the pressures being recorded while the model is somewhat hotter $\left(T_w \approx 0.5T_t\right)$. Although this difference is small in terms of the total temperature, it is undesirable because wall temperature affects both boundary-layer transition and separation. (See ref. 14.) This fact should be kept in mind when examining and comparing the pressure and heating rate distributions.

As noted previously, the model is injected into the tunnel flow for the pressure and heat-transfer runs. The tunnel windows do not extend the full length of the test section

8

immediately above the injection cabin. When the injection system is used, only the forward section of the model is visible through the tunnel windows. In order to obtain schlieren flow photographs of the interaction region, the model has to be mounted directly in the forward part of the tunnel test section, 18 cm upstream of the injection system port. The model wall temperatures for these schlieren photograph runs are similar to those for the pressure runs $\left(T_w \approx 0.5T_t\right)$. In order to show the entire interaction flow region, it is necessary to combine schlieren photographs from two different tunnel runs, one being the tunnel run to obtain the plate pressures and the other being the tunnel run to get schlieren photographs of the interaction region with the model mounted directly in the tunnel.

EXPERIMENTAL RESULTS

Undisturbed Flows

In order to obtain "undisturbed" pressure and heating rate distributions on the flat-plate surface, the wedge shock generator and sting are disconnected from the strut (see fig. 2) and removed. The flat plates are then tested alone to obtain the pressure and heating rate distributions undisturbed by any incident shock waves. These distributions are used in determining undisturbed reference conditions for the pressure rises and heating-rate amplifications caused by the generated shock-wave—boundary-layer interactions.

Curves faired through the measured undisturbed pressure distributions, nondimensionalized with respect to the total pressure for each tunnel run, are plotted in figure 4. The pressures on the plate surface p_1 are 20 to 60 percent larger than the free-stream static pressures p_∞. These increased pressures are caused by the growth of the boundary-layer displacement thickness; they agree within the data scatter shown in figure 4 with other Mach 8 experimental data (ref. 9) and also with weak viscous interaction theory (ref. 29, p. 349). Unfortunately, the undisturbed pressures did not stabilize during the tunnel run for the lowest total pressure $\left(p_t = 480\ 000\ \text{N/m}^2\right)$, and therefore are not plotted. Corresponding to the increased pressures on the plate surface, the local flow Mach numbers M_1 are less than the free-stream Mach numbers listed in table I.

The undisturbed heating rate distributions, expressed in terms of Stanton number N_{St}, are plotted in figure 5. Herein, the Stanton number is

$$N_{St} = \frac{h}{\left(c_p \rho V\right)_1} \tag{4}$$

where c_p, ρ, and V are the specific heat, density, and velocity of the local flow at the outer edge of the boundary layer. The distributions are characteristic of laminar-boundary-layer heating distributions on flat plates and are compared with theoretical

distributions calculated by using an implicit finite-difference scheme of Anderson and Lewis (ref. 30) for laminar boundary layers for the faired experimental pressure distributions. (See fig. 5.)

Interaction Flows

Salient aspects of the pressure and heat-transfer data for the interaction flows are listed in table II for all wedge shock generator angles. The incident shock locations x_i obtained from schlieren flow photographs, are the same for the pressure and heat-transfer runs. The unit free-stream Reynolds numbers per meter are listed for each pressure and heat-transfer tunnel run with the shock generator attached. For the pressure runs the total pressure, the peak pressure rise ratio $P_{pk} \equiv p_{pk}/p_1$, the location of the peak pressure x_{pk}, and the length ℓ of the pressure rise upstream of x_i are indicated. The upstream extent of the pressure rise is nondimensionalized with respect to the calculated (ref. 30) boundary-layer thickness for the undisturbed flow δ_0 at the location where the interaction flow pressure rise starts. (The distance between pressure taps is comparable to the boundary-layer thickness calculated at these locations.) The last two columns list the undisturbed local flow Mach number at the location x_0 and the Reynolds number based on the distance x_0 and local flow conditions. For the heat-transfer runs, the total temperature, the ratio of model wall temperature to total temperature, the peak heating-rate amplification $H_{pk} \equiv h_{pk}/h_1$, the location of the peak heating x_{pk}, and the value of the peak heating rate h_{pk} are indicated.

Schlieren flow photographs for the 1° wedge interactions are shown in figure 6. As described in the last paragraph of the preceding section, it was necessary to combine schlieren photographs from two different tunnel runs in order to show the entire interaction flow region. Detailed observation of the photographs reveals that the wedge-generated shocks initially are stronger than inviscid flow shocks for a 1° wedge, but are bent downstream (weakened) by the bow waves from the plate leading edge. Extending the part of the wedge shock downstream of the plate bow wave to where it would strike the plate surface in the absence of a boundary layer locates what is referred to herein as the incident shock location on the plate surface, x_i. (See fig. 6, $R/m = 1.1 \times 10^6$.)

The pressures measured on the plate surface for these interactions are nondimensionalized with respect to the free-stream total pressure for each tunnel run. The interaction pressure distribution is then taken as the ratio of p/p_t for the disturbed flow to p/p_t for the undisturbed (flat-plate) flow:

$$P \equiv \frac{\left(p/p_t\right)_{disturbed}}{\left(p/p_t\right)_{undisturbed}} \tag{5}$$

10

TABLE II.- SALIENT EXPERIMENTAL RESULTS FOR INTERACTION FLOW

(a) Pressure data

θ, deg	x_i, m	R/m	P_t, MN/m^2	P_{pk}	x_{pk}, m	ℓ/δ_0	M_0	$R_{x,o}$
1	0.253	1.4×10^6	0.53	---	----	--	---	----------
	.260	2.0	.74	1.57	0.332	7	7.03	0.442×10^6
	.269	3.7	1.52	1.55	.343	11	7.39	.818
	.278	6.3	2.86	1.50	.302	14	7.62	1.487
3	0.253	1.3×10^6	0.48	---	----	--	---	----------
	.264	2.0	.77	2.10	0.317	10	7.03	0.410×10^6
	.275	4.0	1.63	2.17	.322	15	7.39	.844
	.283	6.6	3.00	2.35	.332	22	7.62	1.459
5	0.266	1.4×10^6	0.50	---	----	--	---	----------
	.271	1.9	.71	3.30	0.327	13	7.03	0.342×10^6
	.278	3.7	1.50	3.84	.327	20	7.39	.722
	.283	6.4	2.90	4.46	.353	28	7.62	1.280

(b) Heat-transfer data

θ, deg	x_i, m	R/m	T_t, K	T_w/T_t	H_{pk}	x_{pk}, m	h_{pk}, W/m^2-K
1	0.253	1.3×10^6	711	0.412	1.67	0.271	4.67
	.260	1.8	703	.417	1.51	.292	4.46
	.269	3.6	740	.396	1.58	.312	6.33
	.278	6.6	775	.379	1.45	.312	9.05
3	0.253	1.2×10^6	715	0.414	2.75	0.302	6.96
	.264	1.8	712	.415	2.88	.322	7.18
	.275	3.9	737	.400	2.95	.327	10.42
	.283	6.4	767	.385	3.51	.368	15.89
5	0.266	1.3×10^6	730	0.405	4.55	0.302	11.55
	.271	2.0	724	.407	6.75	.368	12.91
	.278	3.6	748	.396	9.98	.373	24.85
	.283	6.5	766	.386	14.05	.373	45.32

This ratio minimizes effects caused by minor variations in p_t from run to run. The undisturbed values of p/p_t are taken from the curves faired through the data (fig. 4) in order to avoid multiplying the data scatter.

Interaction pressure distributions for the 1° shock generator are plotted in figure 7. The unit Reynolds numbers shown are those for the tunnel runs with the shock generator installed. (The unit Reynolds numbers for the corresponding undisturbed flow tunnel runs are shown in fig. 4.) For the smallest Reynolds number run ($R/m = 1.4 \times 10^6$, see table II), the pressures had not stabilized and are not plotted. The plotted pressure ratios start to rise $\left(\text{at } x_o\right)$ considerably upstream of the incident shock locations. The incident shock locations, obtained from examination of the schlieren flow photographs, are indicated by the vertical lines with the appropriate symbol denoting the corresponding unit Reynolds number. The length of the pressure rise upstream of x_i is referred to as "ℓ" herein.

Calculated values of the overall pressure rise ratios $\left(p_3/p_1\right)$ for inviscid flows are indicated by the horizontal dashed lines in figure 7. These values are obtained in the following manner. The measured undisturbed-flow pressures p_1/p_t are used to determine the local Mach number M_1 of the flow over the flat-plate surface in region 1. (See sketch of inviscid flow included in fig. 7.) The incident shock wave angle (downstream of the plate bow wave) is measured from the schlieren flow photographs. This angle and M_1 define the effective deflection of the local flow (from oblique shock relations). Oblique shock relations are then employed in calculating the pressure rise across the incident shock p_2/p_1 and the local Mach number M_2 in region 2. If an inviscid reflection of the incident shock from the plate surface (equal flow deflection angle) is assumed, the pressure rise across the reflected shock p_3/p_2 is calculated for M_2 from oblique shock relations. The pressure ratios p_2/p_1 and p_3/p_2 are multiplied to obtain the overall pressure rise p_3/p_1 across the incident shock and its reflection from the plate surface in the absence of boundary-layer effects.

The peak pressure rise ratios listed in table II are chosen at the locations where the pressure distributions appear to reach their maximum values, exclusive of trailing-edge effects. For example, in figure 7, the three furthest downstream pressure ratio values are excluded. Examination of the corresponding schlieren photographs (fig. 6) reveals the possibility of a compression wave reflecting from the wedge boundary layer and influencing the pressures in the extreme downstream part of the instrumented section of the flat plate.

Both the undisturbed (flat plate) and disturbed flow (interaction) heat-transfer coefficient distributions are plotted in figure 8 for the 1° shock generator. For the lowest unit Reynolds number flow, the heat-transfer coefficient distribution remains essentially unchanged by the interaction until just upstream of the incident shock location. It then

12

rises to a peak value downstream of the incident shock location. Holden (ref. 31) notes that this behavior is characteristic of fully attached, low Reynolds number, relatively thick boundary-layer flows with pressure rises. For the higher Reynolds number flows, the interaction heating rates drop below the undisturbed flow values upstream of the incident shock location. This decrease is associated with the thickening of the laminar boundary layer caused by the interaction. The heating increases to a peak value downstream of the incident shock location. The initial decrease and then sharp increase in the interaction heating distribution for the highest Reynolds number flow is representative of laminar boundary-layer flows approaching separation (ref. 31).

Schlieren flow photographs of the interaction flows for the 3° wedge shock generators are shown in figure 9. The unit Reynolds numbers shown in the schlieren photographs are those corresponding to the photographic tunnel runs; they vary by less than 10 percent from the corresponding unit Reynolds numbers for the pressure and heat-transfer tunnel runs. (See table II.)

Interaction pressure ratio distributions for the 3° wedge shock generators are plotted in figure 10. Similar to the distributions for $\theta = 1^O$, the pressures start to rise well upstream of the incident shock locations. The distributions do not exhibit any plateau regions of nearly constant pressures, but rather show a continuous rise to their maximum values, which is indicative of attached laminar boundary-layer flows approaching separation. (See ref. 31.) The measured pressure rises closely approximate the calculated values of p_3/p_1.

The undisturbed and interaction flow heat-transfer rate coefficient distributions for $\theta = 3^O$ are presented in figure 11. There is a very small region of decreased heating for the lowest Reynolds number interaction. The flow can be classified as fully attached. (See ref. 31.) Particularly evident in the distribution for the highest Reynolds number, the heat-transfer rates continue to increase downstream of the interaction region. This effect can be attributed to the shock interaction disturbing the boundary layer and causing transition.

Data for the largest angle wedge shock generators ($\theta = 5^O$) are presented in figures 12 to 14. The schlieren flow photographs (fig. 12) were scaled to obtain the incident shock angles and the incident shock locations indicated in figure 13. All the pressure distributions rise to values that are fairly well approximated by the calculated values of p_3/p_1.

The interaction heat-transfer coefficient distributions (see fig. 14) are more rounded in the region of decreased heating than for the $\theta = 3^O$ distributions, which exhibit a more cusped shape. Holden (ref. 31) notes that cusped shapes are indicative of flows approaching incipient separation, whereas separated flows exhibit rounded distributions of reduced heating rates. The steady downstream rise of the heating rate

distributions indicates the onset of boundary-layer transition prompted by the disturbance caused by the incident shock wave (ref. 31). Although the Reynolds numbers based on the total instrumented plate length (x = 0.38 m) are less than 2.5×10^6, the disturbance caused by an incident shock wave enhances the onset of boundary-layer transition, particularly for free shear layers. (See ref. 26).

THEORETICAL ANALYSES, COMPARISONS, AND CORRELATIONS

Free Interaction Pressure Rises

Although the maximum pressure rise and the upstream extent of the pressure rise depend strongly on the shock strength, the initial pressure rise should be independent of the mechanism generating the shock wave. This concept of a "free interaction" (defined by Chapman, Kuehn, and Larson (ref. 32)) between the viscid boundary layer and the inviscid external flow in the upstream portion of the interaction region has been well established (refs. 12 and 13).

The pressure ratio distributions from where the ratios start to rise above $P = 1$ to where the ratios begin to diverge for the different wedge shock generator angles are plotted in figure 15. The pressure ratios are plotted against $(x - x_0)/x_0$, where the subscript o indicates undisturbed conditions at the upstream location where the disturbance pressure rise begins. The initial pressure ratio rises are shifted so that they all start at $x = x_0$, and therefore initially follow the same general trend. Of course, the stronger shock generator data approach larger pressure ratio values than do the weaker shock generator data. No consistent Reynolds number trends are apparent.

The effects of the different shock generator angles are eliminated partially by plotting the data in terms of the universal similarity function $F(s)$ suggested by Carrière, Sirieix, and Solignac (ref. 13):

$$F(s) = \left[\frac{2(P - 1)}{\gamma M_0^2} \frac{\Delta \nu}{c_{f,o}} \right]^{1/2} \tag{6}$$

where $s \equiv (x - x_0)/(x_f - x_0)$, $\Delta \nu$ is the change in the Prandtl-Meyer angle for isentropic compression $\Delta \nu = f(P)$, γ is the ratio of specific heats ($\gamma = 1.4$ herein), c_f is the coefficient of friction, subscript o indicates undisturbed conditions at $x = x_0$ (the location where the pressure rise starts), and x_f is a reference location. The location x_f, which scales the extent of the pressure rise, is determined by requiring that $F = 0.81$ at $x = x_f$. This empirical value (F = 0.81 at s = 1.00) has been found (ref. 13) to correlate separated laminar boundary-layer pressure rises well for a wide range of test conditions.

14

In figure 15, the pressure ratio distributions are forced through $P \approx 1$ at $x = x_o$; in figure 16, the distributions are forced through $F = 0.81$ at $x = x_f$. Although the similarity function F does reduce effects of different shock generator angles, there remains an inconsistent Reynolds number effect.

Plateau and Incipient Separation Pressure Rises

As sketched in figure 1, pressure distributions corresponding to shock-induced laminar-boundary-layer separation frequently display a "plateau" region wherein the pressure varies only slightly. Many investigators have postulated that the increase in pressure to the plateau value should be independent of the mechanism causing separation, and that the plateau pressure coefficient should scale with Reynolds number. (See refs. 2 and 14 to 16.) Extensive results from many experiments have been correlated (refs. 2 and 15) to obtain the following expression for the laminar plateau pressure rise:

$$P_{plat} = 1 + \frac{1.2M_1{}^2}{\left[\left(M_1{}^2 - 1\right)R_{sep}\right]^{1/4}} \tag{7}$$

In the preceding expression, R_{sep} is the Reynolds number based on distance from the leading edge to the location of separation. For the current experiments, R_{sep} is based on local flow conditions and the distance x_o. Although there is appreciable scatter in the experimental plateau pressure levels (standard deviation ±10 percent about eq. (7)), the expression is representative of laminar plateau pressure levels for a wide range of test conditions.

Equation (7) is used to calculate the plateau pressure rises shown in table III for the present experiments. Within the accuracy of equation (7) (±10 percent), the calculated

TABLE III.- CALCULATED PLATEAU PRESSURE RATIOS

R/m	P_{plat}
1.9×10^6	1.9
3.7	1.8
6.5	1.7

plateau pressure rises are the same for all three shock generators ($\theta = 1^o$, 3°, and 5°) for each nominal value of the unit Reynolds number. (The plateau pressure is a "weak" function of R_{sep}, which is taken as $R_{x,o}$ herein. The values of the fourth root of $R_{x,o}$ agree within 10 percent for $\theta = 1^o$, 3°, and 5° for each nominal value of the unit

Reynolds number; see table III). In using equation (7), the location of the pressure rise R_{sep} must be known before P_{plat} can be calculated.

If a laminar boundary layer is well separated, then there will be a region of nearly constant pressure (plateau pressure) that can be estimated by using equation (7). The minimum pressure rise required to cause laminar boundary-layer separation (incipient separation) is referred to as the incipient separation pressure rise $\left(P_{incip}\right)$. Values of P_{incip} can be calculated by using oblique shock relations for M_1 and an incipient deflection angle α_{incip} given by (refs. 17 to 20):

$$M_1 \alpha_{incip} = \frac{\lambda M_1^3}{\sqrt{R_{x,i}}} \tag{8}$$

The proportionality constant λ, as given by Ball (ref. 17), is approximately unity for $T_w \approx 0.5 T_t$. As noted above, $T_w \approx 0.5 T_t$ for the pressure data; therefore, $\lambda = 1$ is used in evaluating α_{incip} (radians) from equation (8). Calculated values of the pressure rise ratios required to cause incipient separation are listed in table IV for the four nominal values of the unit Reynolds numbers for the present experiments. The measured

TABLE IV.- CALCULATED PRESSURE RATIOS

FOR INCIPIENT SEPARATION

R/m	P_{incip}
1.3×10^6	2.2
1.9	1.9
3.7	1.7
6.5	1.6

peak pressure rises for the $\theta = 3^\circ$ and 5° interaction flows (see table II) exceed the calculated values of P_{incip}. However, in those present cases where separation does occur, the extent of the reverse flow region is too small to produce a substantial region of nearly constant "plateau" pressures at the calculated levels indicated in table III. (See figs. 10 and 13.)

Upstream Extent of Pressure Rise

The upstream extent of a laminar pressure rise depends on several parameters: the overall strength of the pressure rise, the boundary-layer thickness, wall temperature, the character of the boundary layer at reattachment, and others. (See refs. 21 to 25.) Although there are no adequate empirical methods for reliably predicting the upstream

16

extent of laminar pressure rises for a wide range of conditions (ref. 2), the effects of various parameters on laminar pressure rises can be described at least qualitatively. (See refs. 21 to 25.)

The undisturbed boundary-layer thickness at the start of the pressure rise δ_0 intuitively appears to be appropriate as a scaling length for the upstream extent of the pressure rise caused by an incident shock wave. Values of ℓ/δ_0 from the present experiments (table II) are plotted against overall increases in pressure $P_{pk} - 1$ in figure 17. If the data are examined, a Reynolds number effect becomes apparent. For each of the three shock generator angles, ℓ/δ_0 increases with increasing Reynolds number. This condition leads one to seek a consistent Reynolds number effect.

The initially laminar nature of the boundary layers being considered, the values of ℓ/δ_0 are divided by $\sqrt{R_{x,i}}$ and plotted against $P_{pk} - 1$ in figure 18. The consistency of the results prompts one to seek an exponential variation of the nondimensionalized pressure rise lengths with $P_{pk} - 1$. The resulting equation

$$\frac{\ell/\delta_0}{\sqrt{R_{x,i}}} = \frac{\left(P_{pk} - 1\right)^{0.36}}{75} \tag{9}$$

is plotted in figure 18; all the present data fall very close to this curve.

Equation (9) is empirical and is based only on the present data, which are weak incident shock waves interacting with initially[3] laminar boundary layers on a sharp flat plate for $7 < M_0 < 8$, $0.5 \times 10^6 < R_{x,i} < 2.0 \times 10^6$, and $T_w \approx 0.5T_t$. Within this range of conditions, equation (9) accounts for boundary-layer thickness, Reynolds number, and pressure rise effects. Indeed, the trends of ℓ with δ_0, $R_{x,i}$, and P_{pk} suggested by equation (9) are similar to those suggested by other investigators. (See refs. 21 to 25.) However, the equation does not account for wall temperature, Mach number, transition, and other effects that strongly influence the extent of a laminar pressure rise. (See refs. 16 to 25, 33 and 34.) Data from other sources, included in figure 18, do not correlate from the values given by equation (9). The data presented by Watson, Murphy, and Rose (ref. 33) were obtained for $R_{x,i} \approx 750\ 000$. Their Mach 5.7 data were obtained for a ratio of wall temperature to total temperature of approximately 0.41; their Mach 5.8 data were obtained for a ratio of wall temperature to total temperature of approximately 0.36. The data point from Ball (ref. 21) was obtained for $R_{x,i} = 330\ 000$ and $T_w/T_t = 0.56$. The data of Gray and Rhudy (ref. 16) were obtained for adiabatic wall temperatures for $60\ 000 < R_{x,i} < 1\ 000\ 000$. All the data shown in figure 18 are for weak shock interactions $\left(P_{pk} < 10\right)$. Data obtained for stronger shocks (such as those presented by Holden

---

[3] The undisturbed boundary layers are laminar over the flat-plate surface.

(ref. 31)) differ greatly from the values indicated by equation (9), depending on wall temperature, Mach number, and other effects.

Peak Heating Correlations

Although many investigations (refs. 5 to 11) have been directed toward obtaining correlations of peak heating rates with peak pressures, there is an unacceptably large discrepancy in the results for laminar boundary layers. This discrepancy is evidenced by a large variation in the values of the exponent n in the simplest, and most frequently sought, correlation (refs. 6, 7, 9, and 11):

$$H_{pk} \propto \left(P_{pk}\right)^n \tag{10}$$

Values of n proposed by various investigators are listed in table V.

TABLE V.- PROPOSED VALUES OF EXPONENT IN CORRELATION

OF PEAK HEATING WITH PRESSURE (EQ. (10))

Investigators	Suggested n
Markarian (ref. 6)	1.29
Neumann and Burke (ref. 7)	0.50
Haslett et al. (ref. 9)	.70
Hung and Barnett (ref. 11)	1.13

Values of peak heating amplifications obtained during the present experiments (see table II) are plotted against measured peak pressure rises in figure 19. Many other data points, presented by Hung (ref. 35), are included in the figure. The large data scatter apparent in the figure precluded obtaining a reliable, simple correlation in the form of equation (10). Hung and Barnett (refs. 11 and 35) have suggested modifying equation (10) by using a simple Reynolds number function instead of a proportionality constant. However, examination of the present data shown in figure 19 reveals no consistent Reynolds number effects. Many investigators have noted large data scatter when attempting simple correlations in the form of equation (10) for laminar flows, and have attributed the scatter to transition occurring near reattachment of the free shear layer. (See refs. 2, 8, 9, 11, and 35.) However, transition in the free shear layer depends on the strength of the pressure rise as well as on Reynolds number. (See refs. 9 and 26.) Therefore, one

would not expect a function of Reynolds number alone to correct satisfactorily the simple correlation[4] shown in equation (10).

Another correlation, suggested by Bushnell and Weinstein (ref. 5), is

$$\frac{h_{pk}}{\rho_w V_e c_p} \propto \left(\frac{\rho_w V_e \delta_{sl}}{\mu_w \sin \phi}\right)^{-0.5} \tag{11}$$

where ρ_w, V_e, and μ_w pertain to the reattached flow, δ_{sl} is the thickness of the shear layer at reattachment, ϕ is the turning angle of the flow at reattachment, and the subscript e refers to conditions at the outer edge of the boundary layer. The data presented by Bushnell and Weinstein were measured at the reattachment of separated flows on trailing-edge flaps. Keyes and Morris (ref. 10) used the same correlation parameters (eq. (11)) for incident shock wave interactions and obtained a larger proportionality constant than that obtained by Bushnell and Weinstein for the flap reattachment data. The correlation presented by Keyes and Morris passes through the present data for incident shock interactions, as shown in figure 20. There is considerable scatter about the correlation line shown in figure 20. In addition to important transition effects, wall temperatures are different for the pressure and heat-transfer data $\left(T_w \approx 0.5 T_t \text{ for pressure data, } T_w \approx 0.4 T_t \text{ for heat-transfer data}\right)$. Although wall temperature effects are known to be particularly important for laminar boundary layers (ref. 25), these effects could not be investigated by using the present model.

CONCLUDING REMARKS

Pressure and heat transfer distributions were obtained on a flat plate in the vicinity of incident shock wave interactions with initially laminar boundary layers. The incident shock strengths ranged from those insufficient to cause separation to those sufficient to cause moderate extents of separated flows. The nominal free-stream Mach number was 8, and Reynolds numbers, based on plate length, ranged from 0.46×10^6 to 2.5×10^6.

The pressure and heating rate distributions generally follow the established trends for nonseparated flows, incipient separation, and laminar free interaction pressure rises. The data support previously derived expressions for the minimum pressure rise required to cause separation (incipient separation). However, there are no well-developed plateau pressure regions in the measured interaction pressure distributions. The upstream extent of the pressure rise, divided by the undisturbed boundary-layer thickness, scales

---

[4] This is contrary to shock wave interactions with turbulent boundary layers; for turbulent flows the simple correlation $H_{pk} = \left(P_{pk}\right)^{0.85}$ is valid for a wide range of flow conditions (ref. 36).

with $\left(P_{pk} - 1\right)^{0.36}$ $\left(\text{where } P_{pk} \text{ is the peak pressure ratio}\right)$ and the square root of the Reynolds number.

The heat-transfer measurements were obtained while the wall temperature was lower than it was for the pressure measurements. Furthermore, the disturbance caused by the incident shock wave usually caused boundary-layer transition prior to the end of the interaction region. These factors strongly affect laminar boundary layers. The present data do not support previously proposed, simple correlations of peak heating with peak pressure.

Langley Research Center,
National Aeronautics and Space Administration,
Hampton, Va., November 4, 1974.

REFERENCES

1. Ryan, B. M.: Summary of the Aerothermodynamic Interference Literature. Tech. Note 4061-160, Naval Weapons Center (China Lake, Calif.), Apr. 1969.

2. Hill, William G., Jr.: A Comparison of Theory and Experiment for Laminar Separation Ahead of a Compression Corner at Supersonic and Low Hypersonic Speeds. Rep. RE-401, Res. Dep., Grumman Aerospace Corp., Dec. 1970.

3. Murphy, John D.: A Critical Evaluation of Analytic Methods for Predicting Laminar Boundary-Layer, Shock-Wave Interaction. NASA TN D-7044, 1971.

4. Korkegi, Robert H.: Survey of Viscous Interactions Associated With High Mach Number Flight. AIAA J., vol. 9, no. 5, May 1971, pp. 771-784.

5. Bushnell, Dennis M.; and Weinstein, Leonard M.: Correlation of Peak Heating for Reattachment of Separated Flows. J. Spacecraft & Rockets, vol. 5, no. 9, Sept. 1968, pp. 1111-1112.

6. Markarian, C. Franklyn: Heat Transfer in Shock Wave – Boundary Layer Interaction Regions. NWC, TP 4485, U.S. Navy, Nov. 1968. (Available from DDC as AD 849 532.)

7. Neumann, Richard D.; and Burke, Gerald L.: The Influence of Shock Wave-Boundary Layer Effects on the Design of Hypersonic Aircraft. AFFDL-TR-68-152, U.S. Air Force, Mar. 1969. (Available from DDC as AD 686 738.)

8. Neumann, Richard D.: Recent Notes and Data on Interference Heating. AFFDL-TR-72-12, U.S. Air Force, May 1972.

9. Haslett, Robert A.; Kaufman, Louis G., II; Romanowski, Richard F.; and Urkowitz, Michael: Interference Heating Due to Shock Impingement. AFFDL-TR-72-66, U.S. Air Force, July 1972.

10. Keyes, J. Wayne; and Morris, Dana J.: Correlations of Peak Heating in Shock Interference Regions at Hypersonic Speeds. J. Spacecraft & Rockets, vol. 9, no. 8, Aug. 1972, pp. 621-623.

11. Hung, F. T.; and Barnett, D. O.: Shockwave-Boundary Layer Interference Heating Analysis. AIAA Paper No. 72-237, Jan. 1973.

12. Lewis, John E.; Kubota, Toshi; and Lees, Lester: Experimental Investigation of Supersonic Laminar, Two-Dimensional Boundary-Layer Separation in a Compression Corner With and Without Cooling. AIAA J., vol. 6, no. 1, Jan. 1968, pp. 7-14.

13. Carrière, P.; Sirieix, M.; and Solignac, J. L.: Similarity Properties of the Laminar or Turbulent Separation Phenomena in a Non-Uniform Supersonic Flow. Applied Mechanics, M. Hetényi and W. G. Vincenti, eds., Springer-Verlag, 1969, pp. 145-157.

14. Johnson, Charles B.: Pressure and Flow-Field Study at Mach Number 8 of Flow Separation on a Flat Plate With Deflected Trailing-Edge Flap. NASA TN D-4308, 1968.

15. Bertram, Mitchel H.; and Henderson, Arthur, Jr.: Some Recent Research With Viscous Interacting Flow in Hypersonic Streams. Proceedings of the 1969 Symposium on Viscous Interaction Phenomena in Supersonic and Hypersonic Flow. Univ. of Dayton Press, c.1970, pp. 1-30.

16. Gray, J. Don; and Rhudy, R. W.: Investigation of Flat-Plate Aspect Ratio Effects on Ramp-Induced, Adiabatic, Boundary-Layer Separation at Supersonic and Hypersonic Speeds. AEDC-TR-70-235, U.S. Air Force, Mar. 1971. (Available from DDC as AD 719 747.)

17. Ball, K. O. W.: Wall Temperature Effect on Incipient Separation. AIAA J., vol. 5, no. 12, Dec. 1967, pp. 2283-2284.

18. Needham, David A.: A Note on Hypersonic Incipient Separation. AIAA J., vol. 5, no. 12, Dec. 1967, pp. 2284-2285.

19. Stollery, J. L.: Hypersonic Viscous Flow Over Concave and Convex Surfaces. Proceedings of the 1969 Symposium on Viscous Interaction Phenomena in Supersonic and Hypersonic Flow, Univ. of Dayton Press, c.1970, pp. 181-212.

20. Holden, Michael S.: Theoretical and Experimental Studies of the Shock Wave-Boundary Interaction on Curved Compression Surfaces. Proceedings of the 1969 Symposium on Viscous Interaction Phenomena in Supersonic and Hypersonic Flow, Univ. of Dayton Press, c.1970, pp. 213-270.

21. Ball, Karlheinz O. W.: An Investigation of the Extent of Laminar Two-Dimensional Boundary Layer Separation at Moderately Hypersonic Speeds. Proceedings of the 1969 Symposium on Viscous Interaction Phenomena in Supersonic and Hypersonic Flow, Univ. of Dayton Press, c.1970, pp. 551-566.

22. Pate, S. R.: Investigation of Flow Separation on a Two-Dimensional Flat Plate Having a Variable-Span Trailing-Edge Flap at $M_\infty = 3$ and 5. AEDC-TRD 64-14, U.S. Air Force, Mar. 1964.

23. Popinski, Z.: Shock Wave-Boundary Layer Interaction. Proceedings of the Third International Heat Transfer Conference — Vol. II, Amer. Inst. Chem. Eng., Aug. 1966, pp. 262-273.

24. Roberts, Melvin L.: Transitional Flow Separation Upstream of a Compression Corner. J. Spacecraft & Rockets, vol. 7, no. 9, Sept. 1970, pp. 1113-1117.

25. Gray, J. Don; and Rhudy, R. W.: Effects of Blunting and Cooling on Separation of Laminar Supersonic Flow. AIAA J., vol. 11, no. 9, Sept. 1973, pp. 1296-1301.

26. Birch, Stanley F.; and Keyes, J. Wayne: Transition in Compressible Free Shear Layers. J. Spacecraft & Rockets, vol. 9, no. 8, Aug. 1972, pp. 623-624.

27. Stainback, P. Calvin; Wagner, Richard D.; Owen, F. Kevin; and Horstman, Clifford C.: Experimental Studies of Hypersonic Boundary-Layer Transition and Effects of Wind-Tunnel Disturbances. NASA TN D-7453, 1974.

28. Schaefer, William T., Jr.: Characteristics of Major Active Wind Tunnels at the Langley Research Center. NASA TM X-1130, 1965.

29. Hayes, Wallace D.; and Probstein, Ronald F.: Hypersonic Flow Theory. Academic Press, Inc., 1959.

30. Anderson, E. C.; and Lewis, C. H.: Laminar or Turbulent Boundary-Layer Flows of Perfect Gases or Reacting Gas Mixtures in Chemical Equilibrium. NASA CR-1893, 1971.

31. Holden, Michael S.: Leading-Edge Bluntness and Boundary-Layer Displacement Effects on Attached and Separated Laminar Boundary Layers in a Compression Corner. AIAA Paper No. 68-68, Jan. 1968.

32. Chapman, Dean R.; Kuehn, Donald M.; and Larson, Howard K.: Investigation of Separated Flows in Supersonic and Subsonic Streams With Emphasis on the Effect of Transition. NACA Rep. 1356, 1958. (Supersedes NACA TN 3869.)

33. Watson, Earl C.; Murphy, John D.; and Rose, William C.: Investigation of Laminar and Turbulent Boundary Layers Interacting With Externally Generated Shock Waves. NASA TN D-5512, 1969.

34. Kaufman, L. G., II; Meckler, L.; and Hartofilis, S. A.: An Investigation of Flow Separation and Aerodynamic Controls at Hypersonic Speeds. J. Aircraft, vol. 3, no. 6, Nov.-Dec. 1966, pp. 555-561.

35. Hung, F. T.: Interference Heating Due to Shock Wave Impingement on Laminar Boundary Layers. AIAA Paper No. 73-678, July 1973.

36. Johnson, Charles B.; and Kaufman, Louis G., II: Interference Heating From Interactions of Shock Waves With Turbulent Boundary Layers at Mach 6. NASA TN D-7649, 1974.
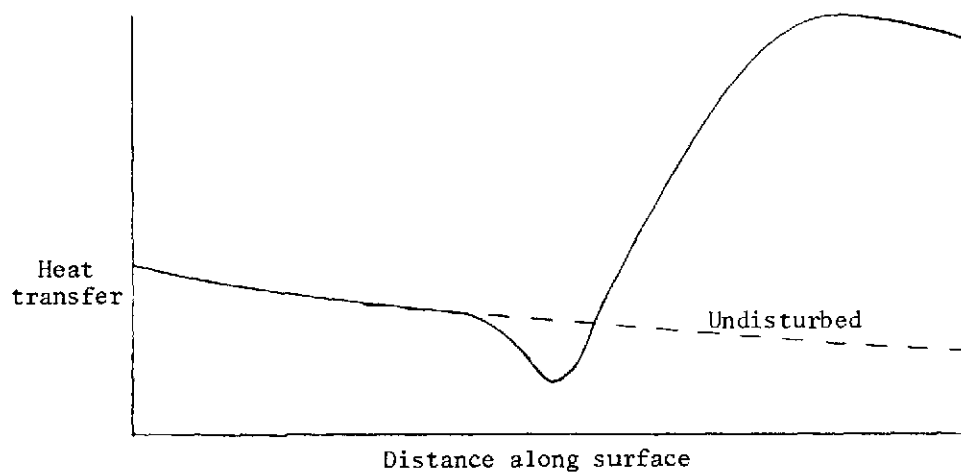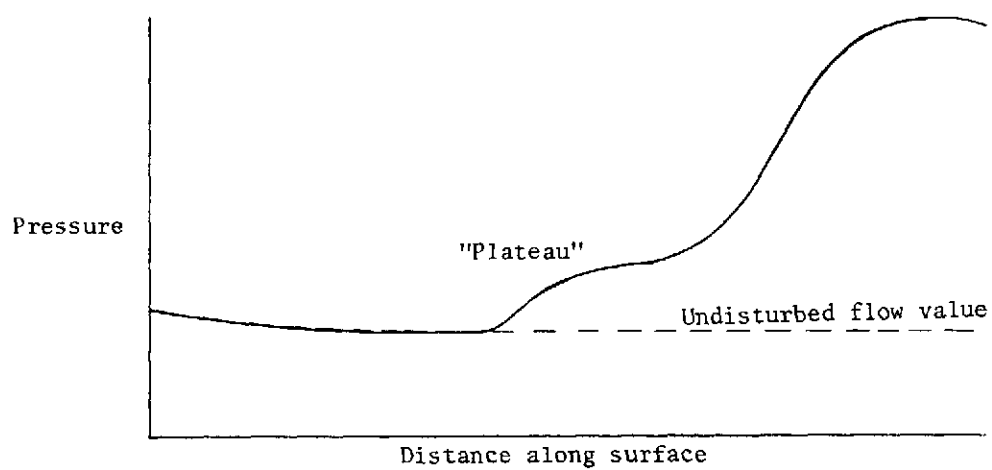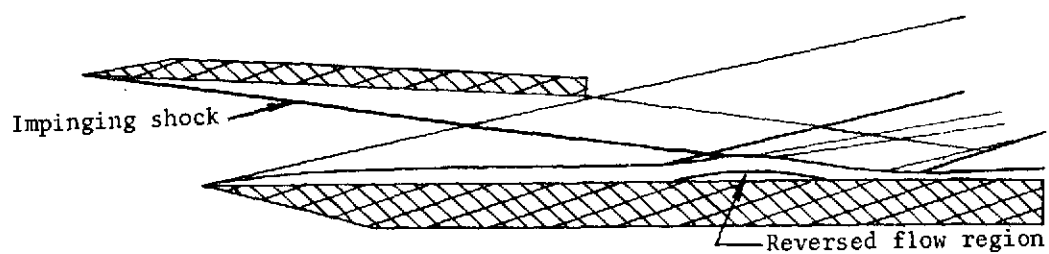
Figure 1.- Sketches of interaction flow and attendant pressure
and heat-transfer distributions.
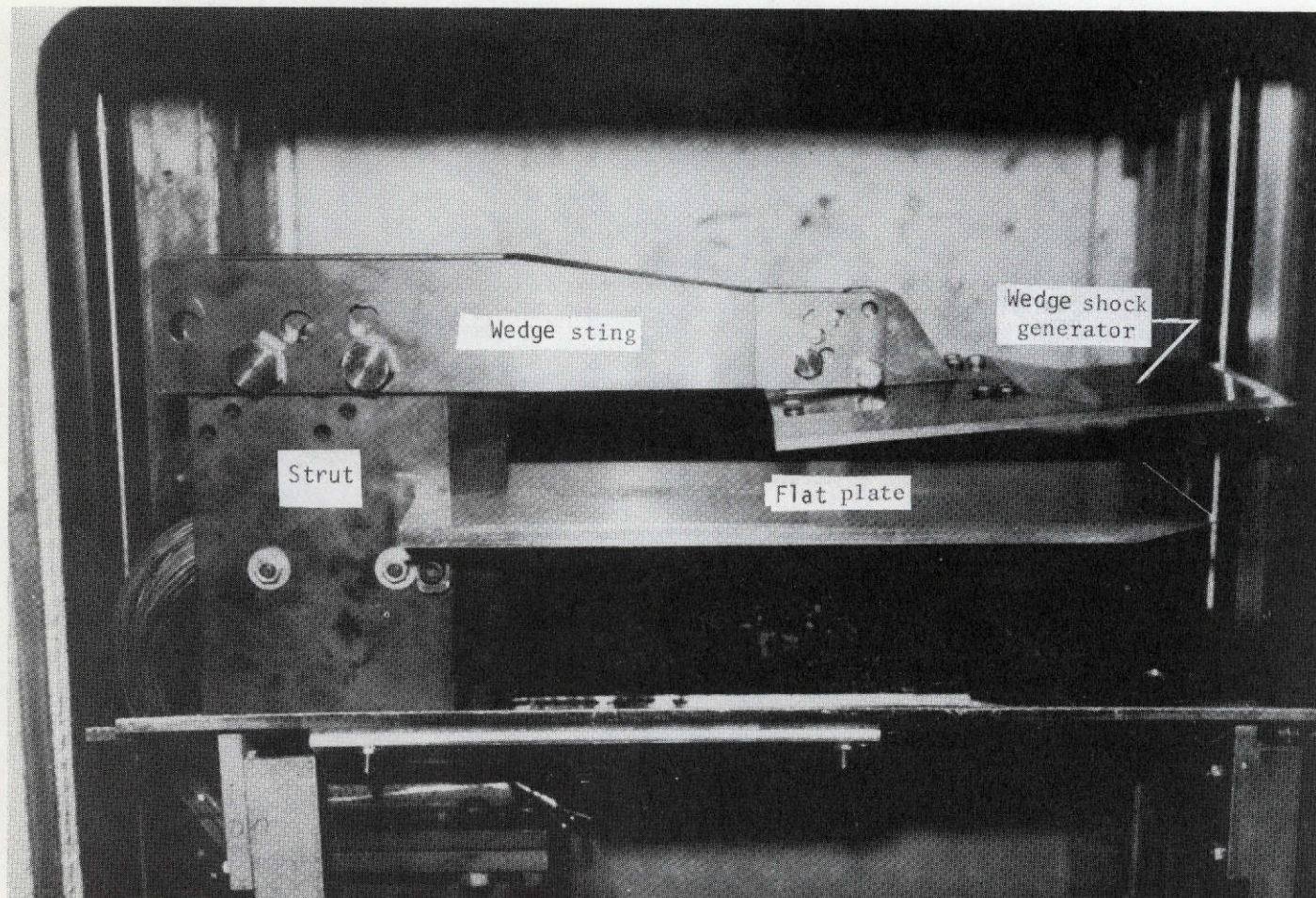
L-74-1162

(a) Model closeup.

Figure 2.- Photographs of model in Mach 8 variable-density tunnel.
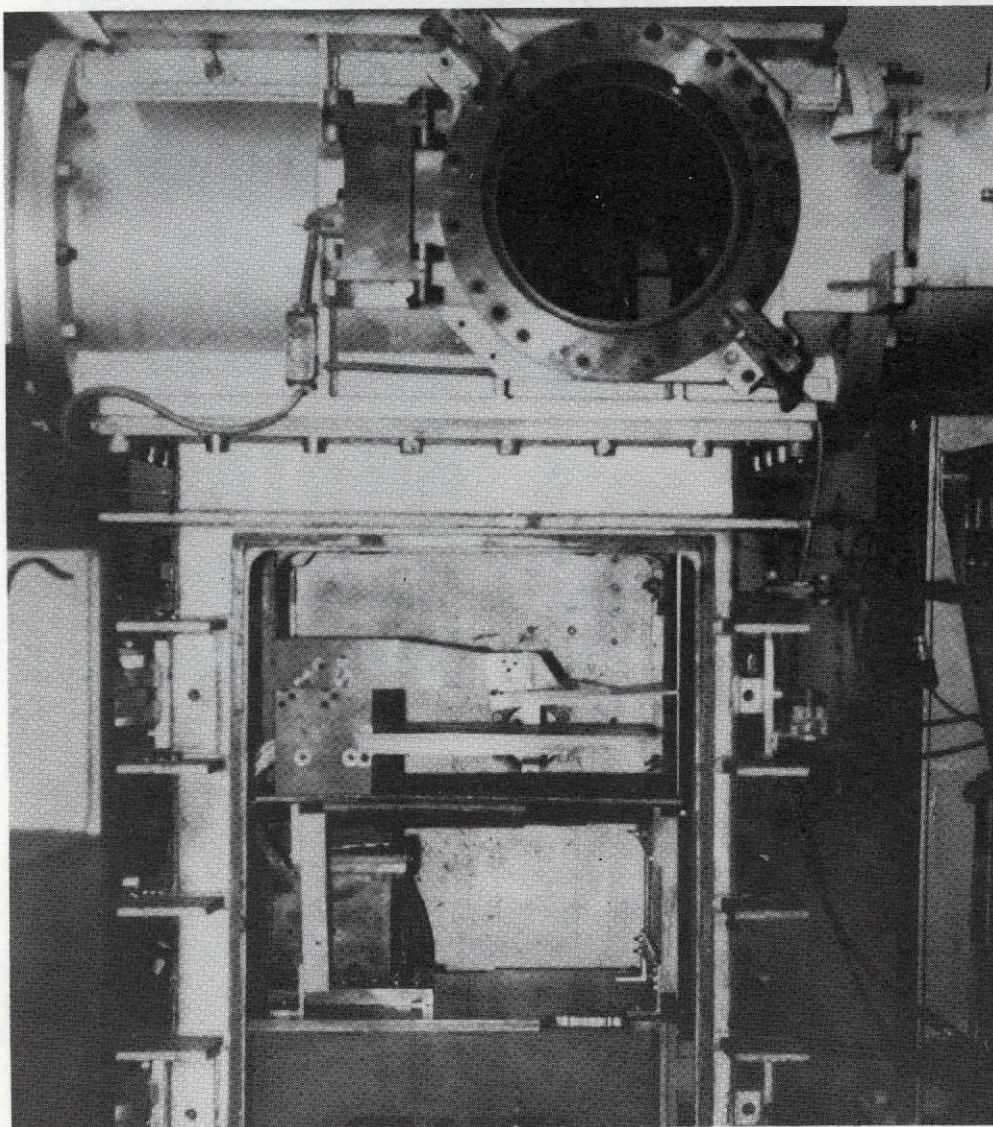
L-74-1163

(b) Model in injection system chamber beneath test section.

Figure 2.- Continued.
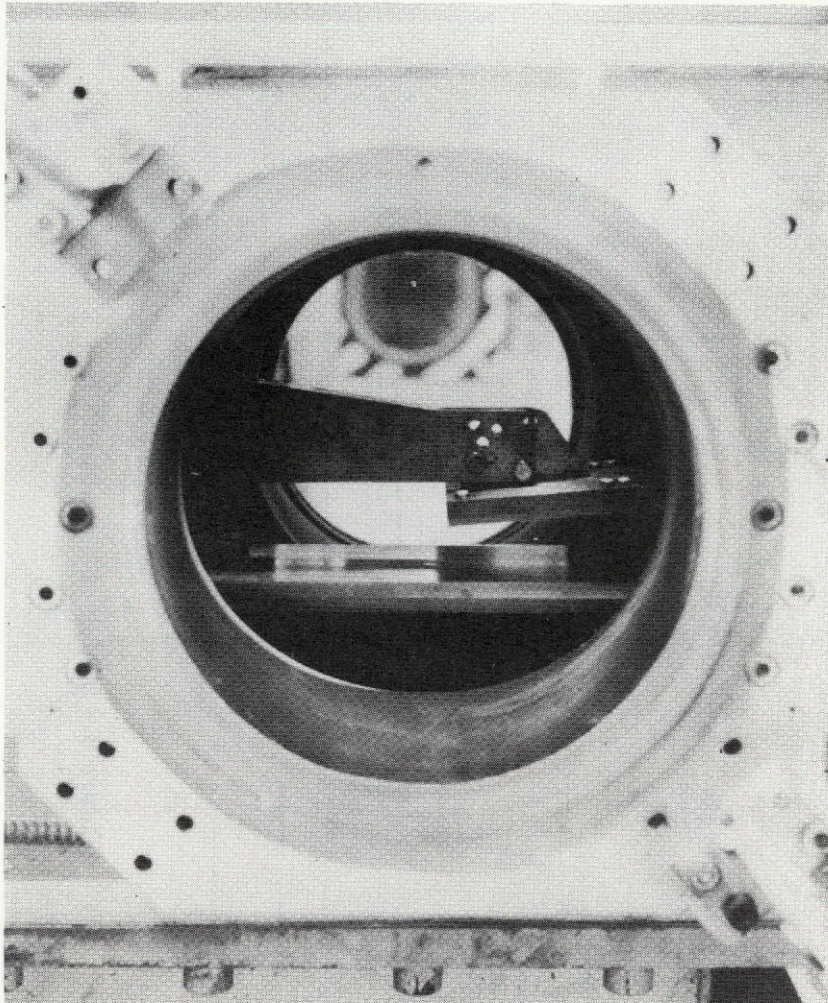
L-74-1164

(c) Model in forward position in test section.

Figure 2.- Concluded.
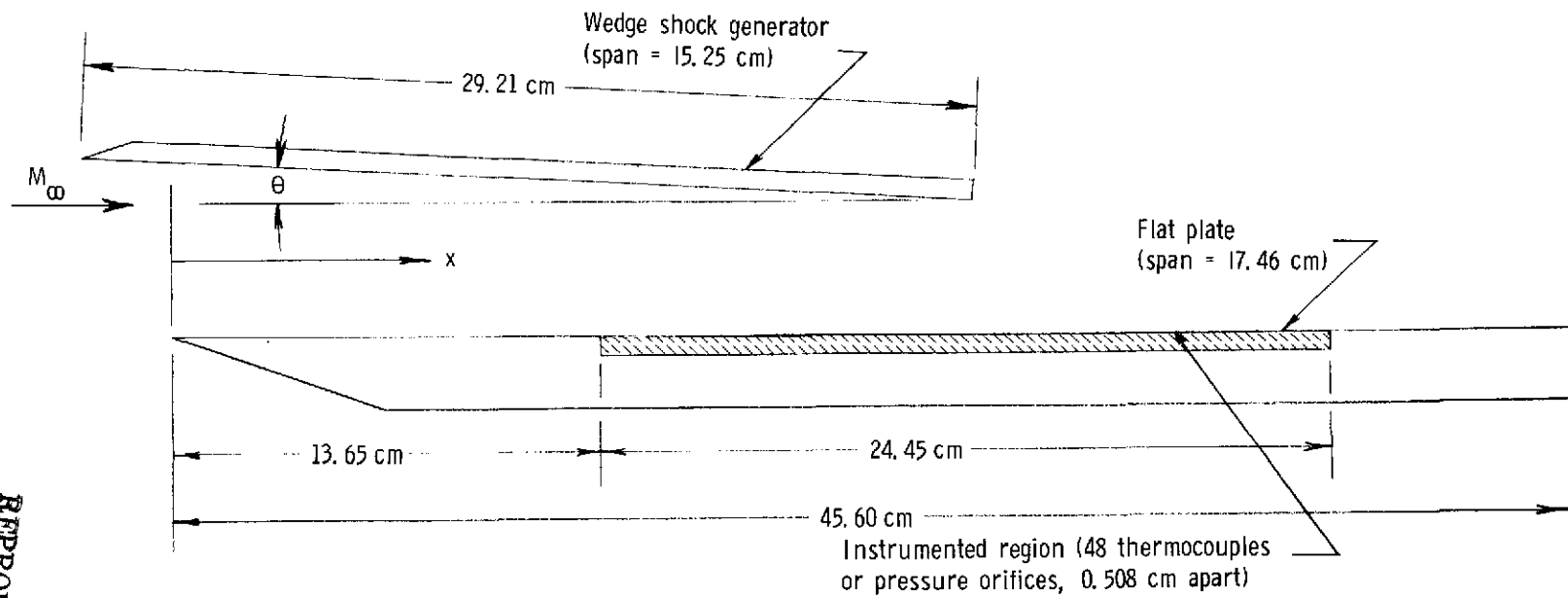
Figure 3.- Sketch of model profile.
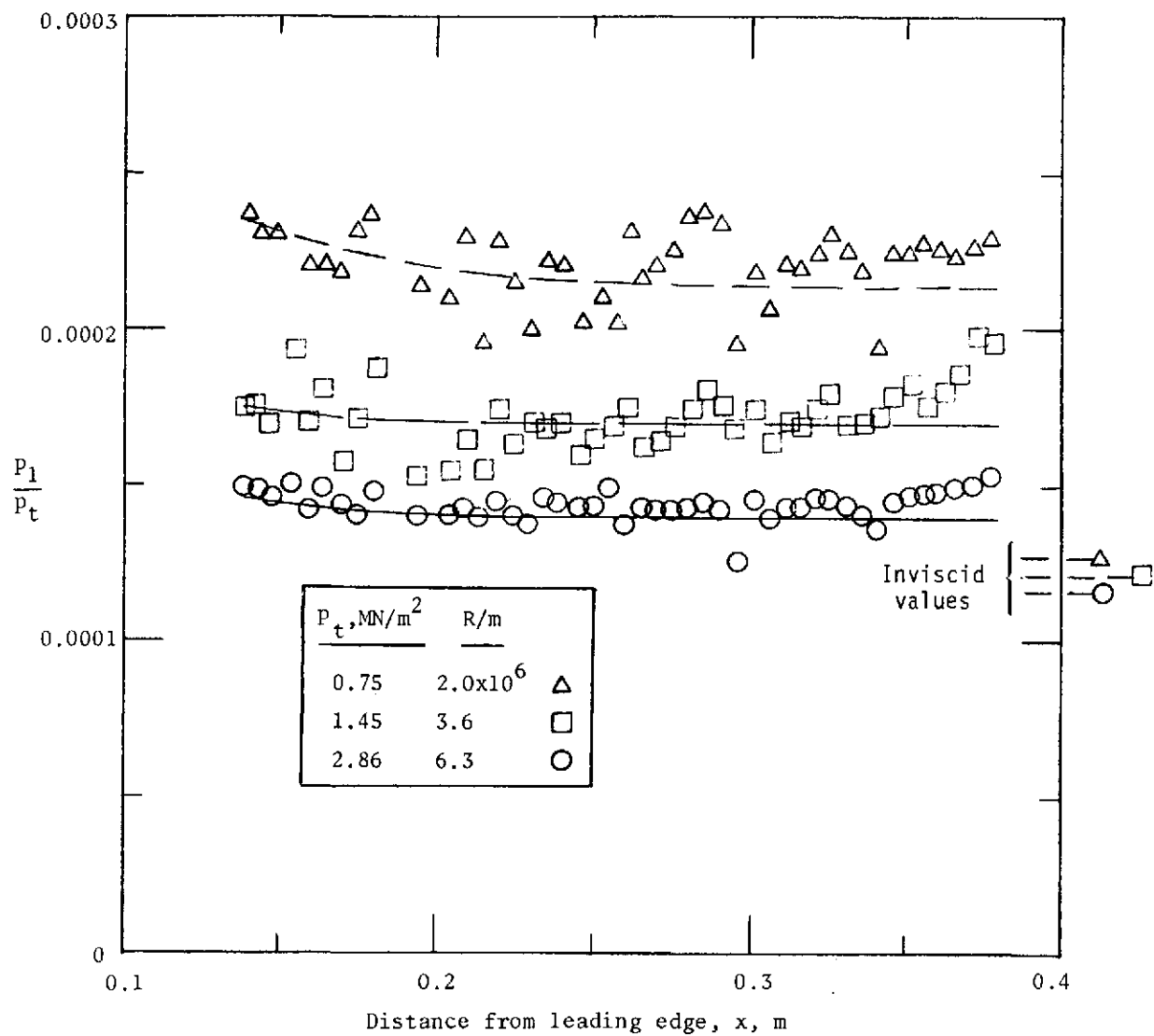
Figure 4.- Curves faired through undisturbed pressure distributions $\left(p_1/p_t\right)$ measured along the flat-plate center line.
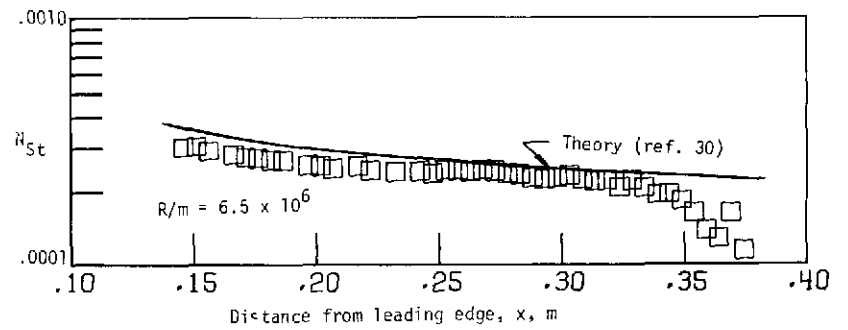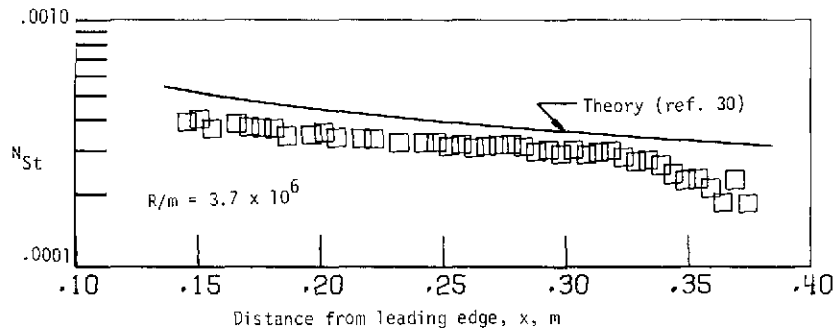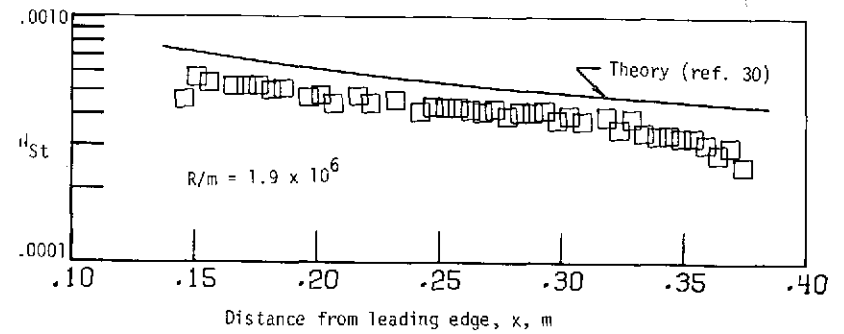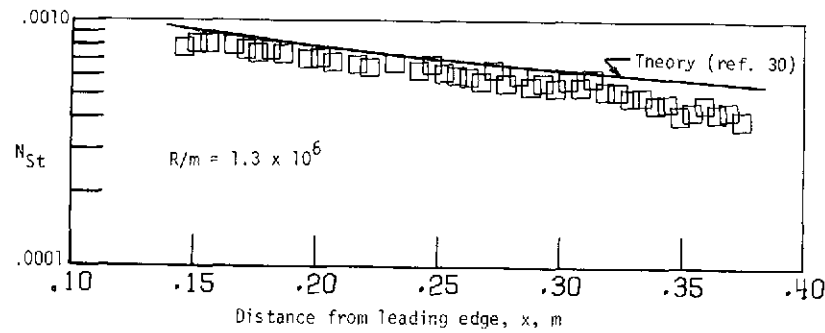
Figure 5.- Undisturbed Stanton number distributions.
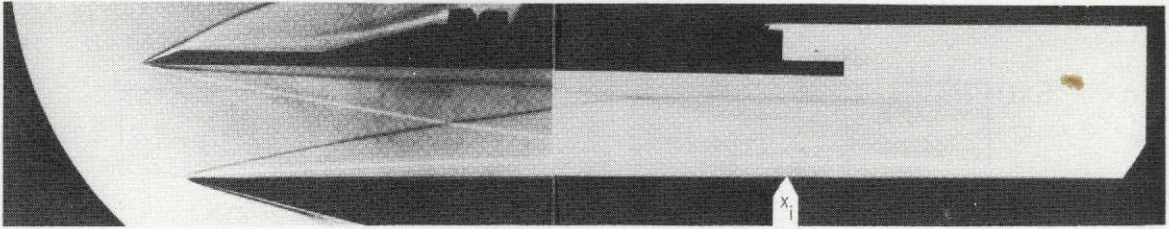
R/m = 1.1×10^6
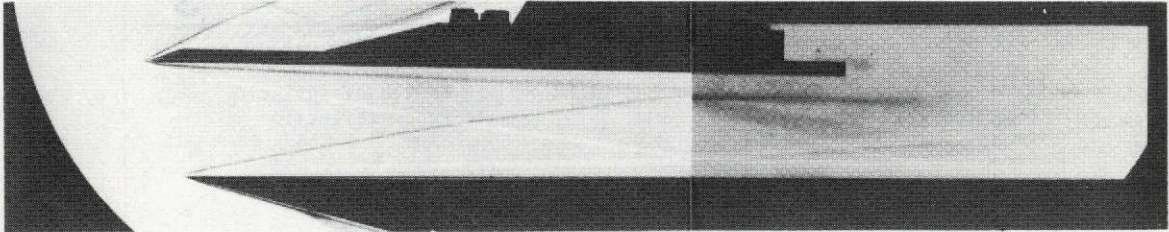
R/m = 2.0×10^6
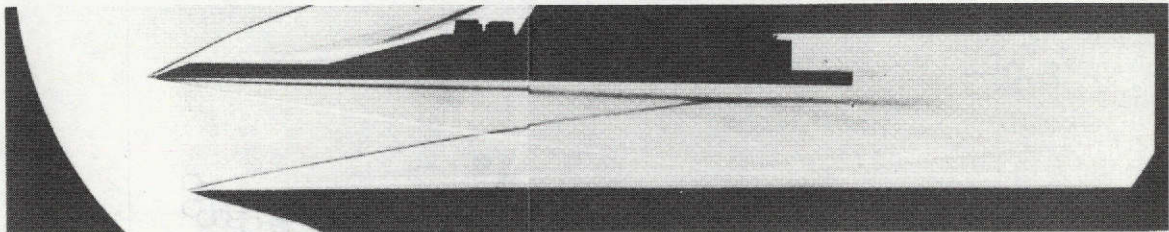
R/m = 3.7×10^6
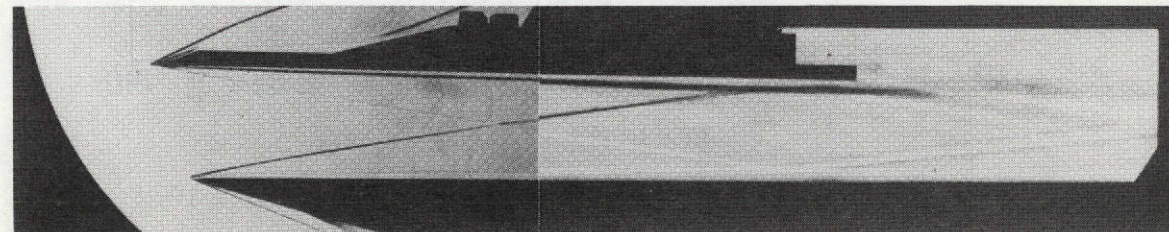
R/m = 6.4×10^6

L-74-1165

Figure 6.- Schlieren flow photographs for $\theta = 1^o$.
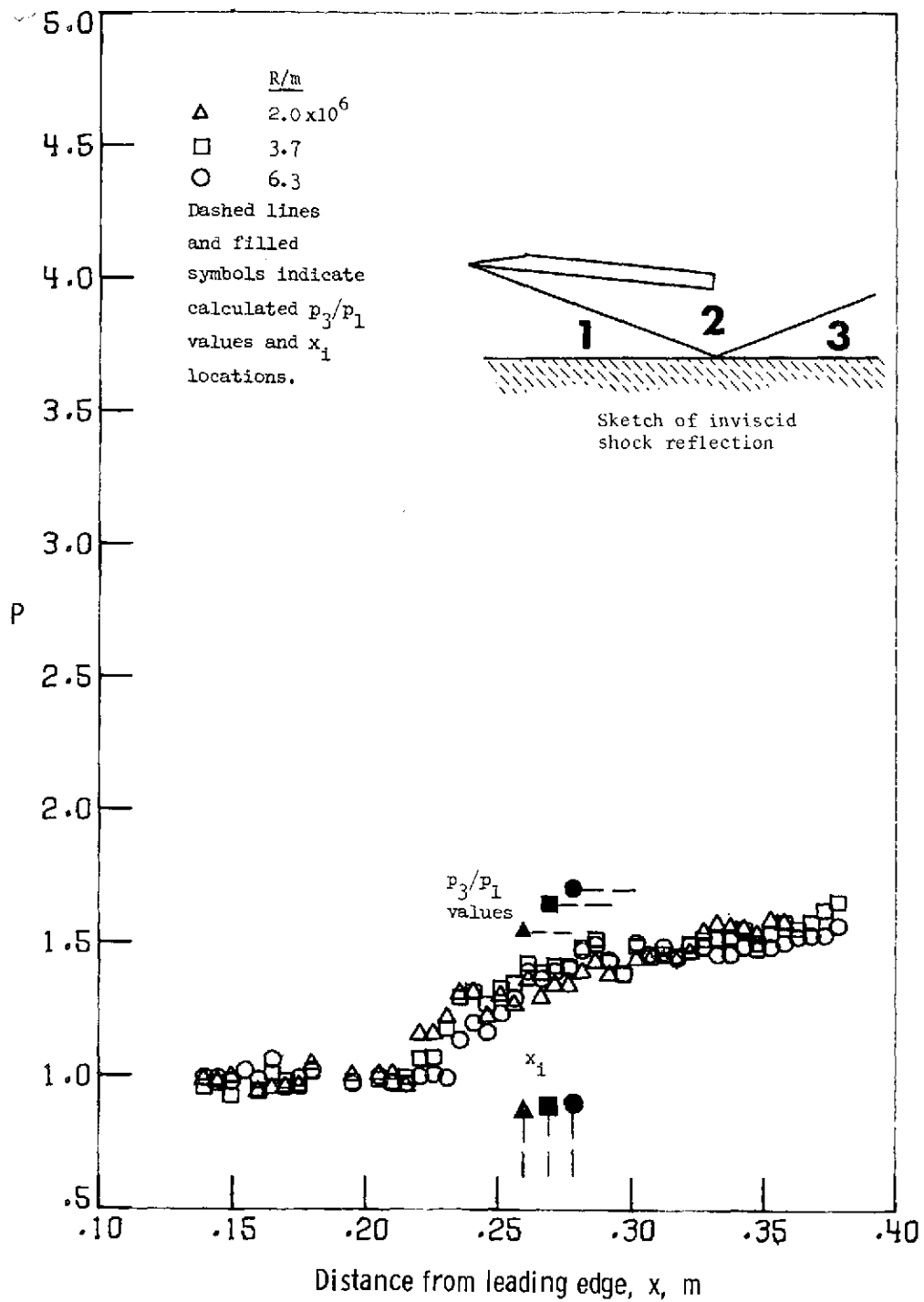
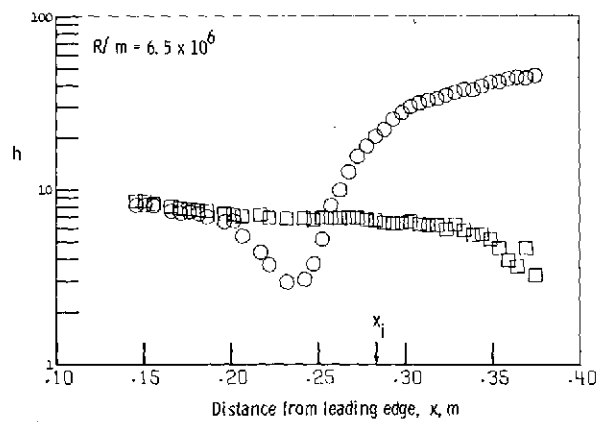Figure 7.- Interaction pressure ratio distributions for $\theta = 1^o$.
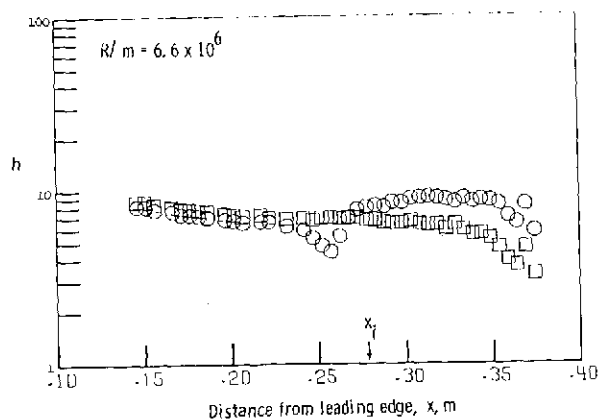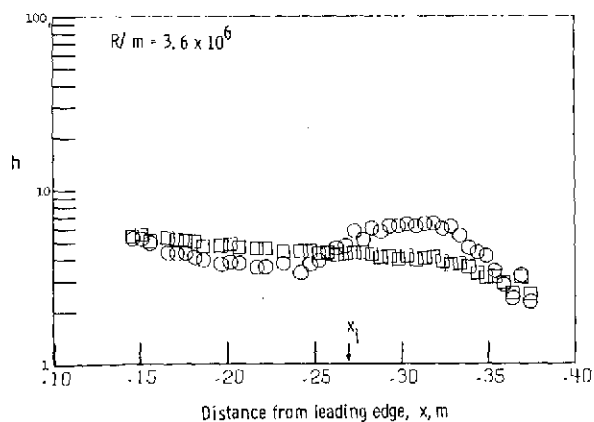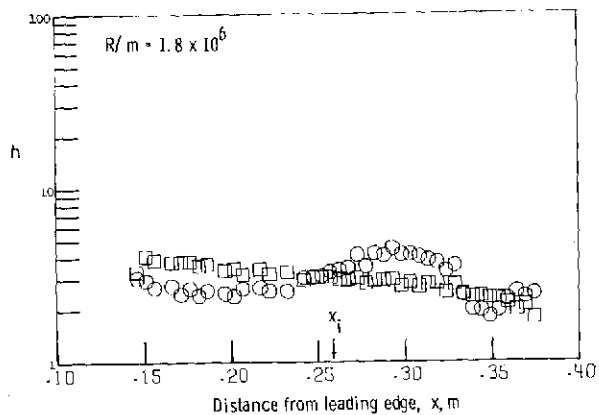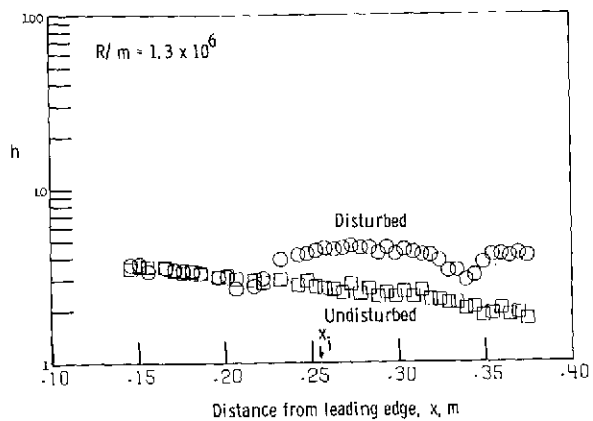
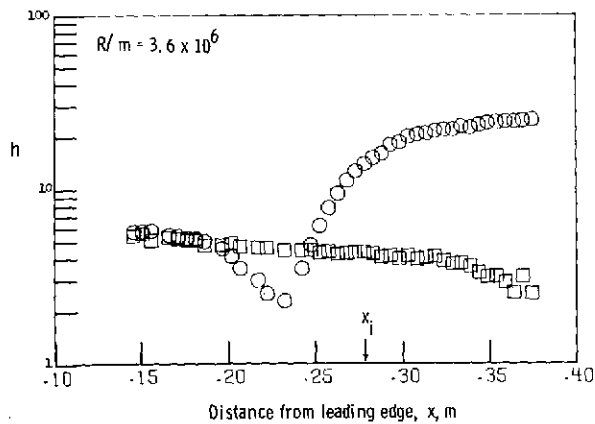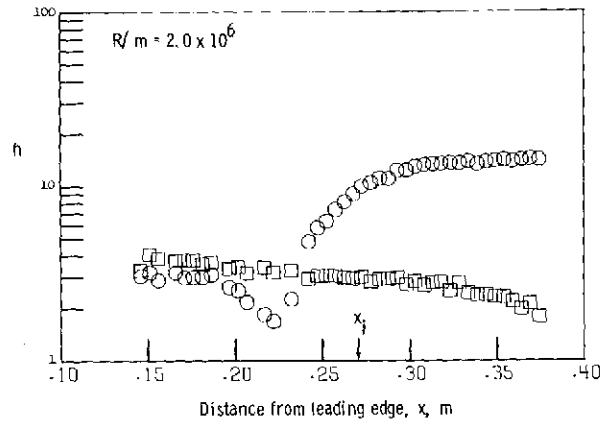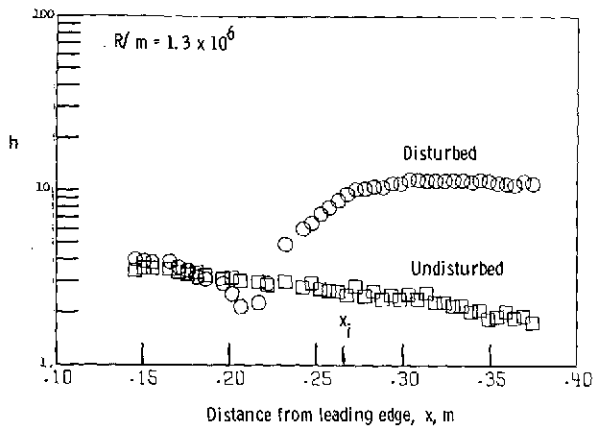**Figure 8.-** Heat-transfer coefficient distributions for $\theta = 1^O$.
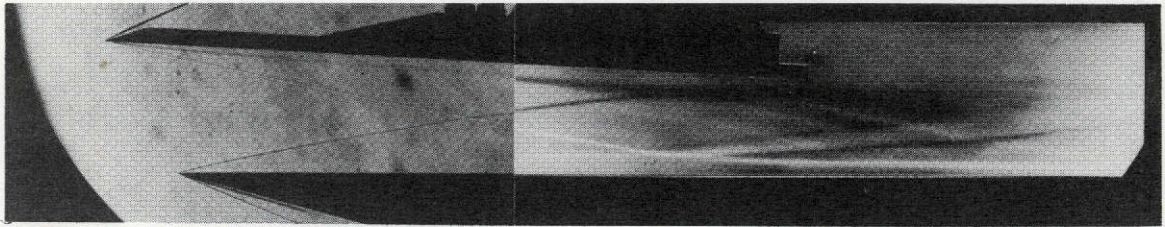
R/m = 1.2 × 10⁶
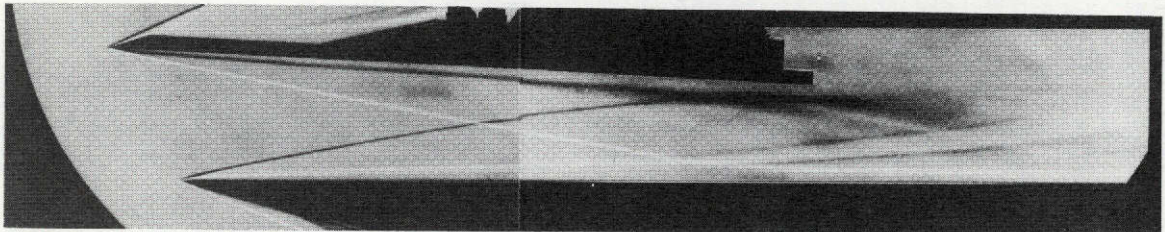
R/m = 1.9 × 10⁶
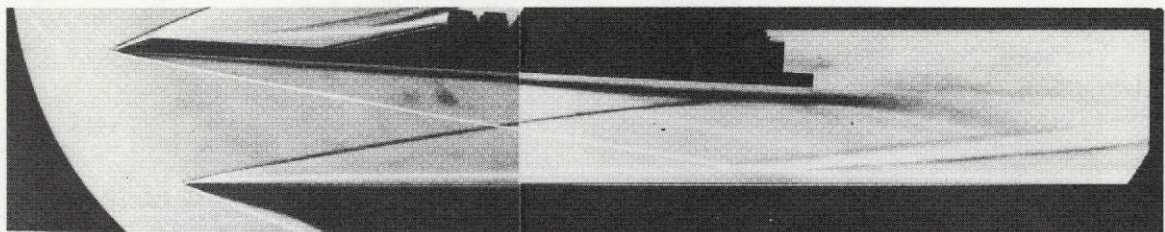
R/m = 3.7 × 10⁶
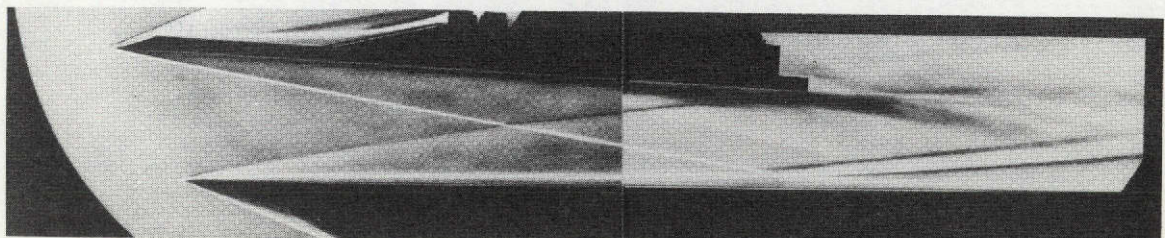
R/m = 6.7 × 10⁶

L-74-1166

Figure 9.- Schlieren flow photographs for $\theta = 3^O$.
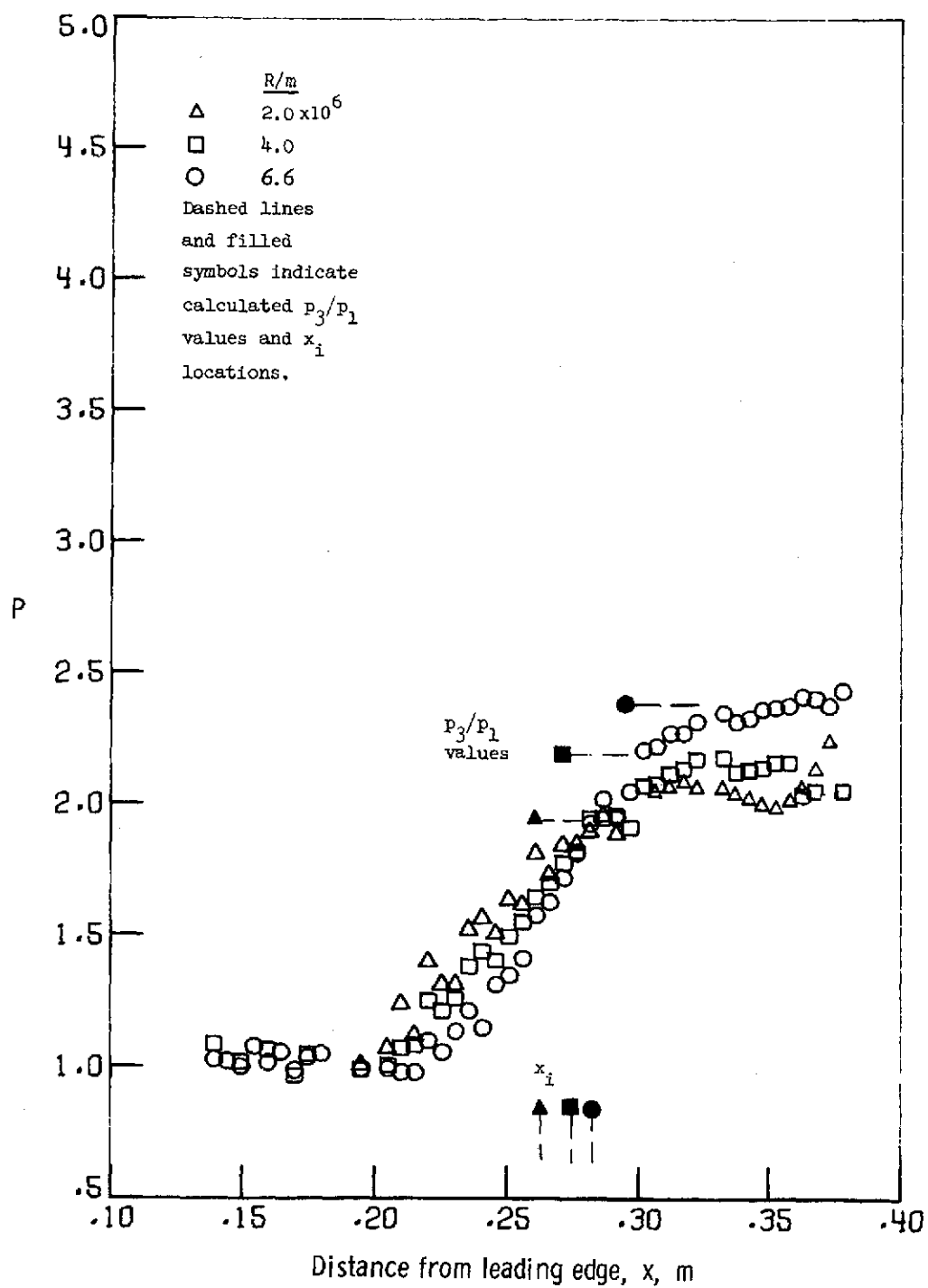
Figure 10.- Interaction pressure ratio distributions for $\theta = 3^o$.
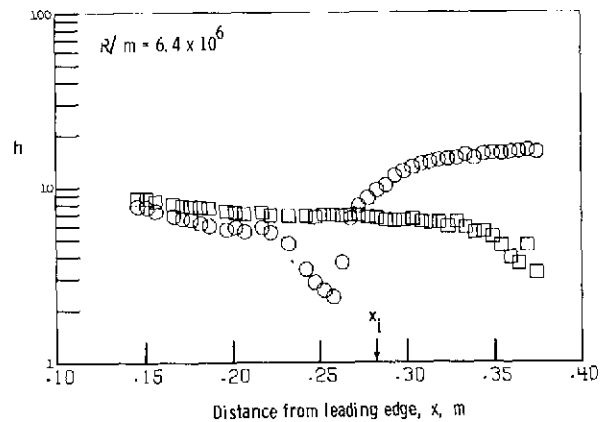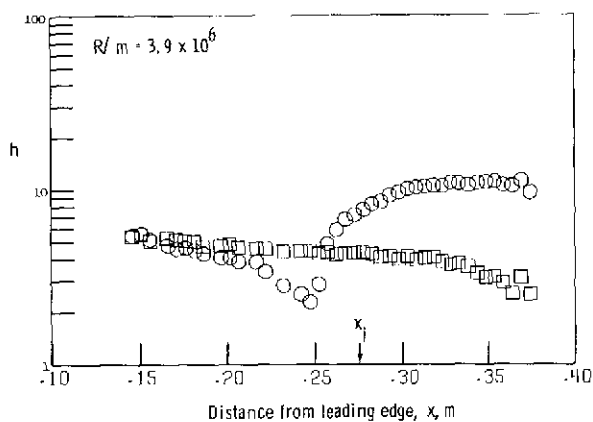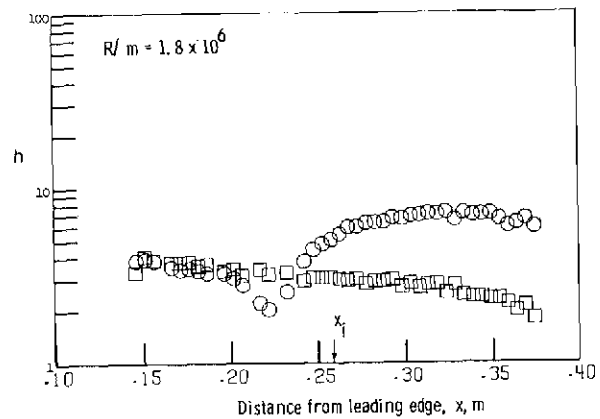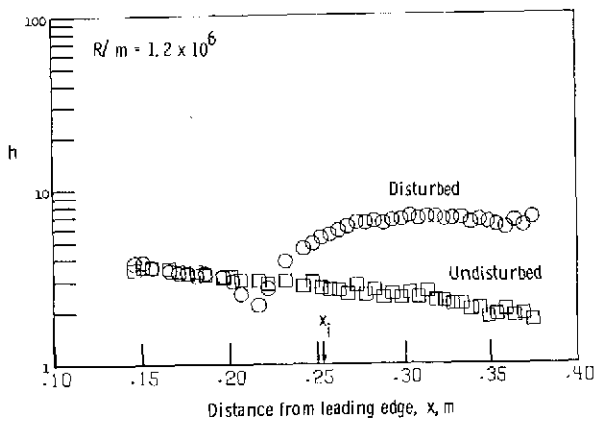
Figure 11.- Heat-transfer coefficient distributions for $\theta = 3^{\circ}$.
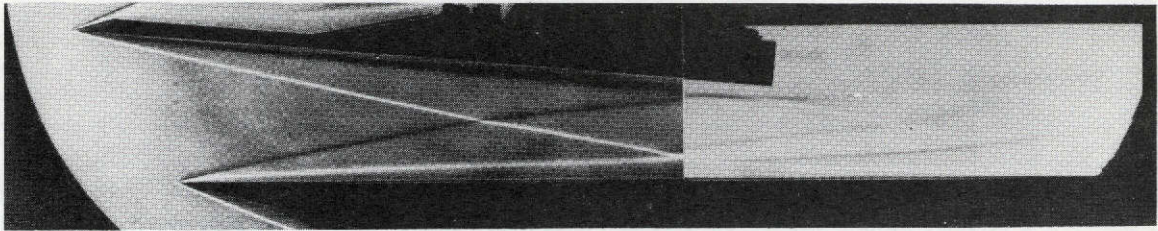
R/m = 1.2×10^6
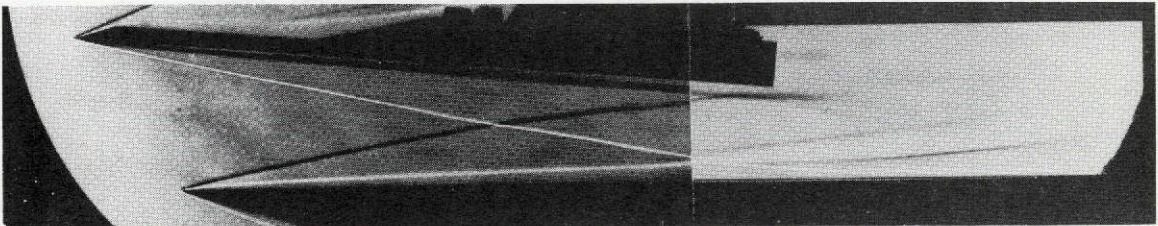
R/m = 2.1×10^6
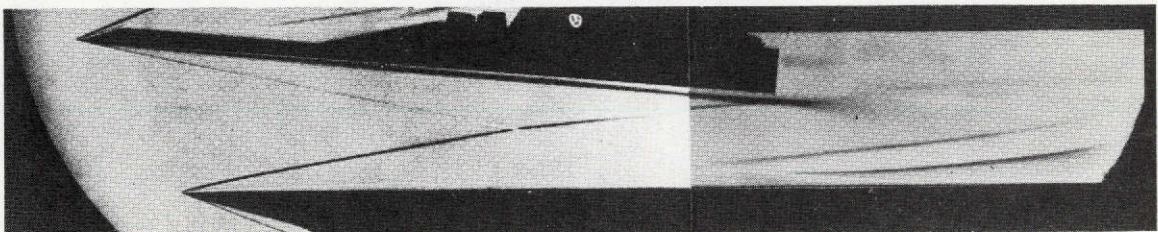
R/m = 3.7×10^6
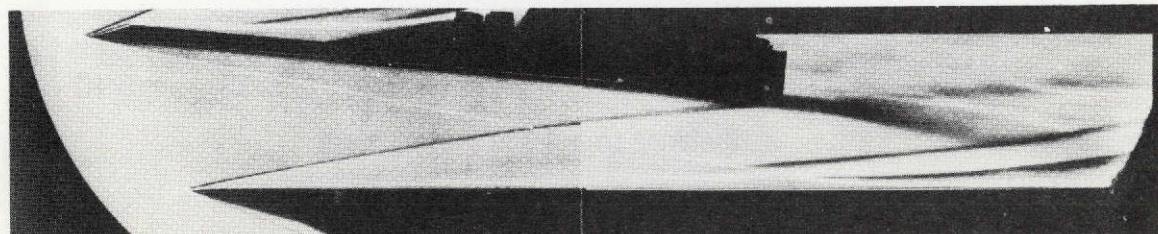
R/m = 6.6×10^6

L-74-1167

Figure 12.- Schlieren flow photographs for $\theta = 5^0$.
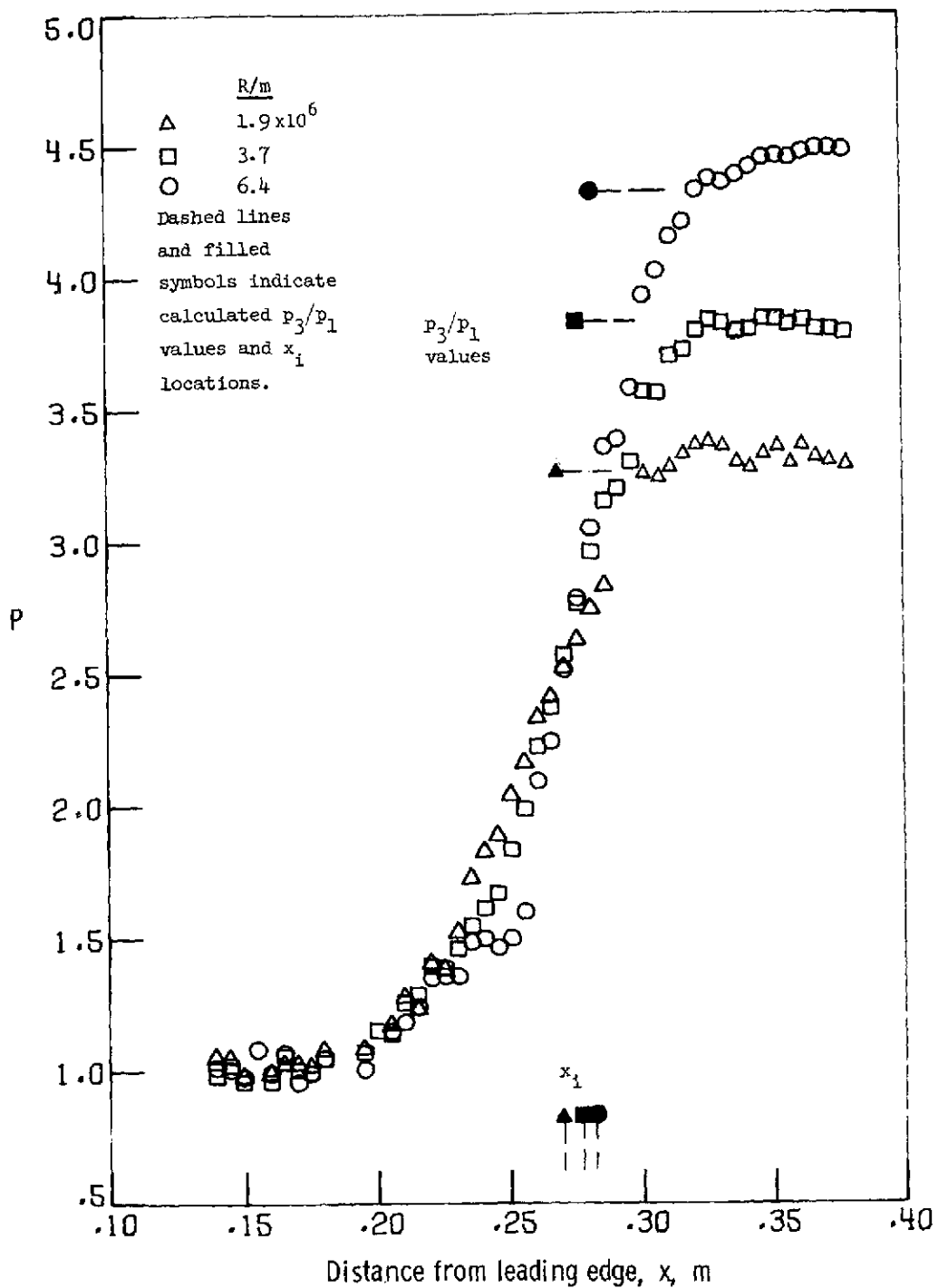
Figure 13.- Interaction pressure ratio distributions for $\theta = 5^{o}$.

Figure 14.- Heat-transfer coefficient distributions for $\theta = 5^\circ$.
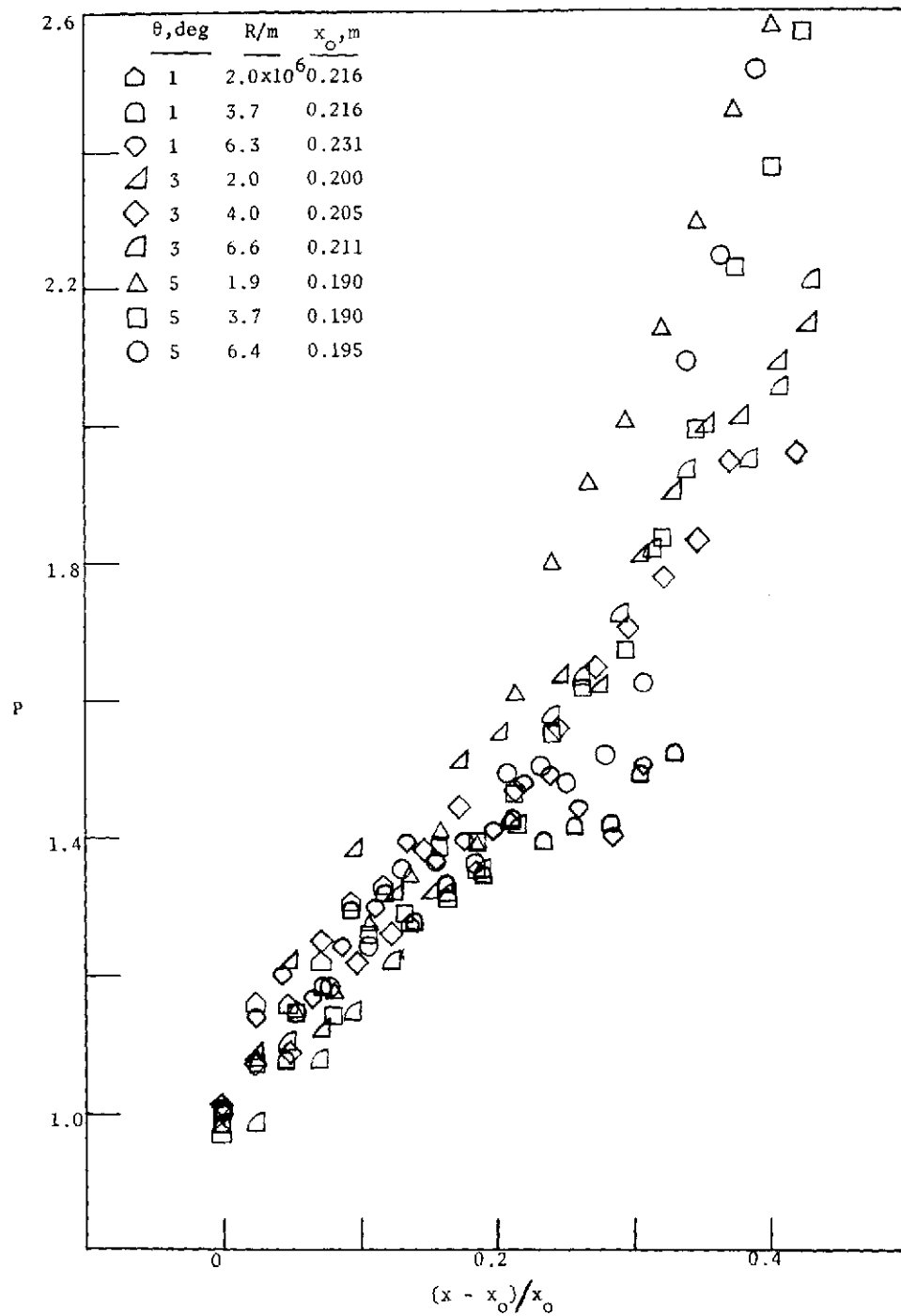
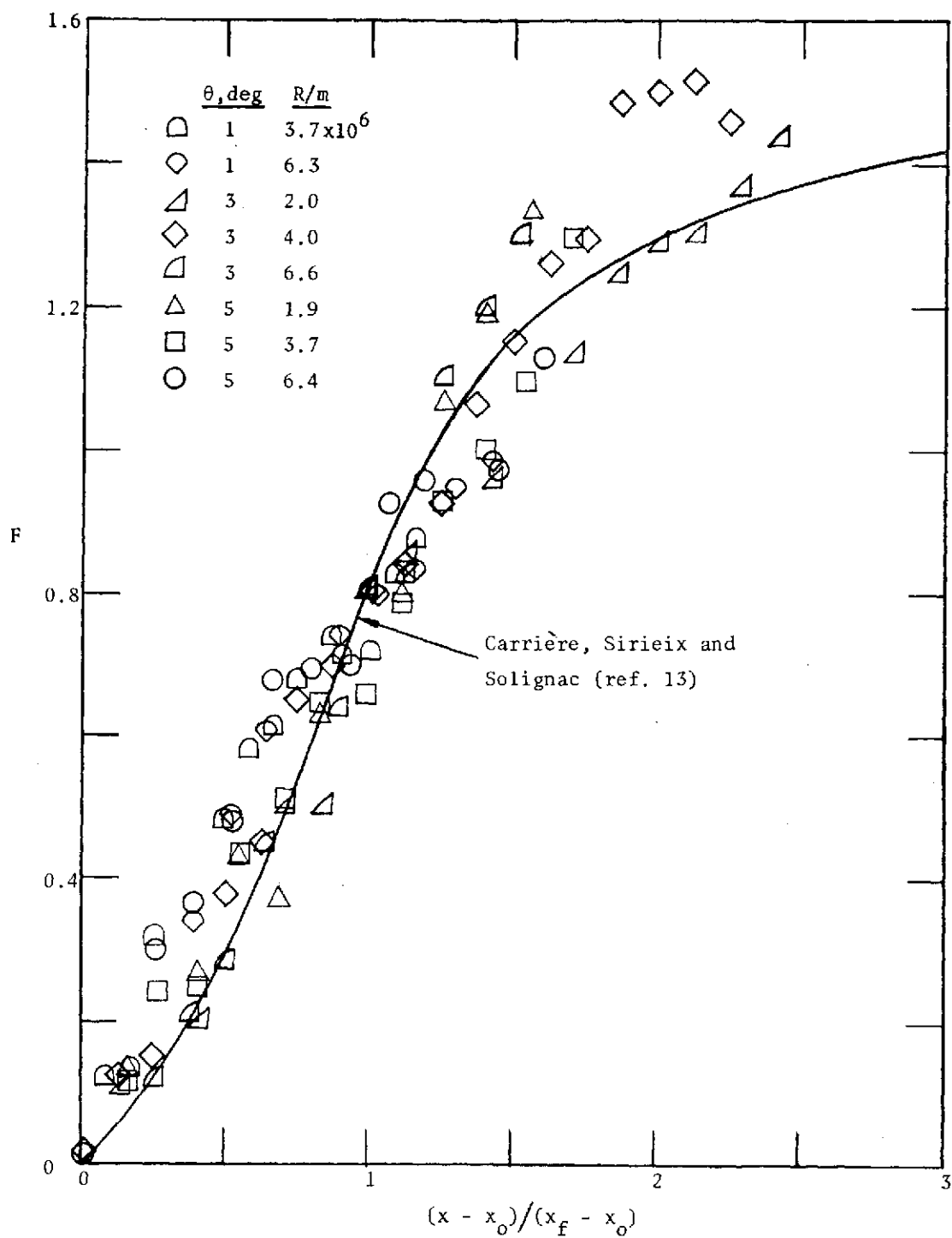Figure 15.- Initial portions of interaction pressure ratio rises.

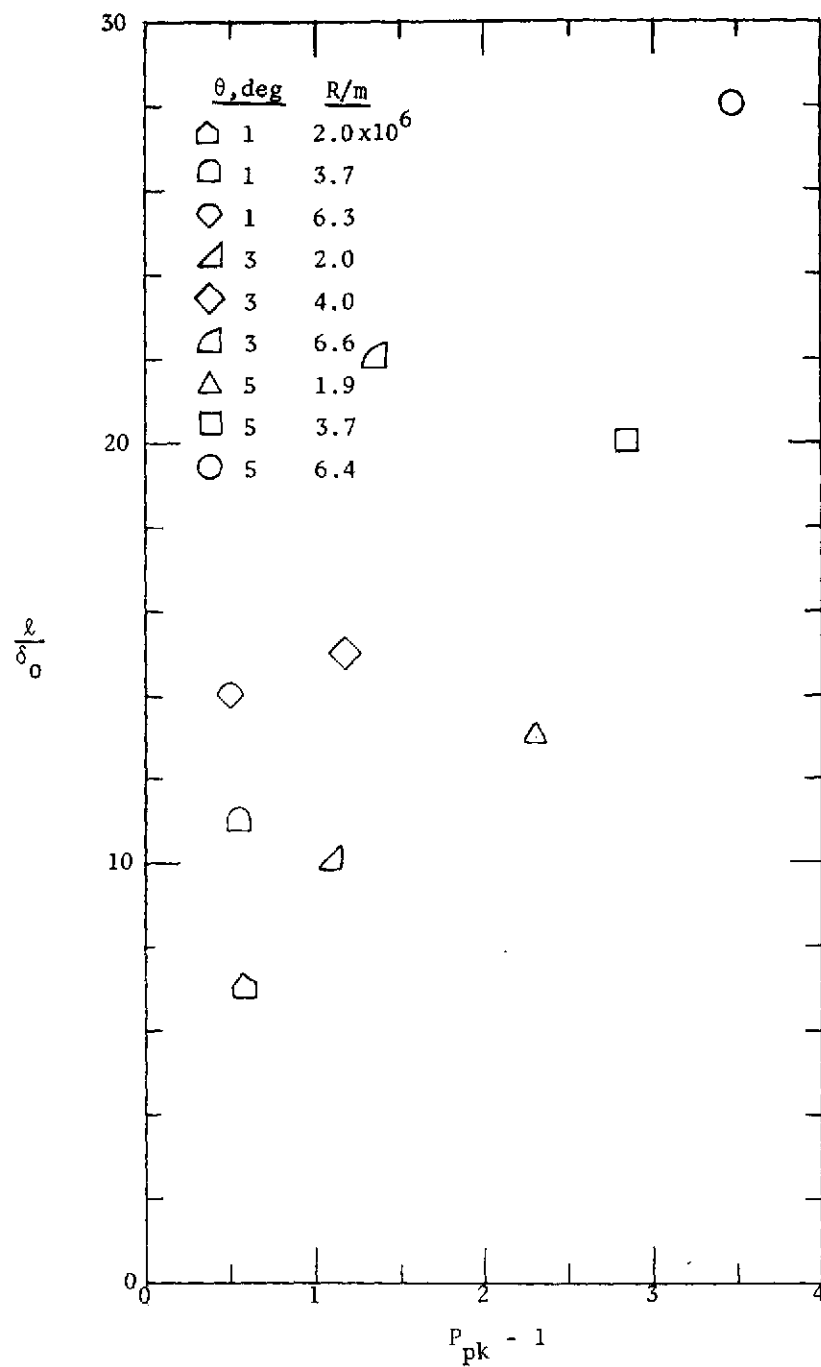Figure 16.- Laminar free interaction pressure rises. (F defined in eq. (6).)

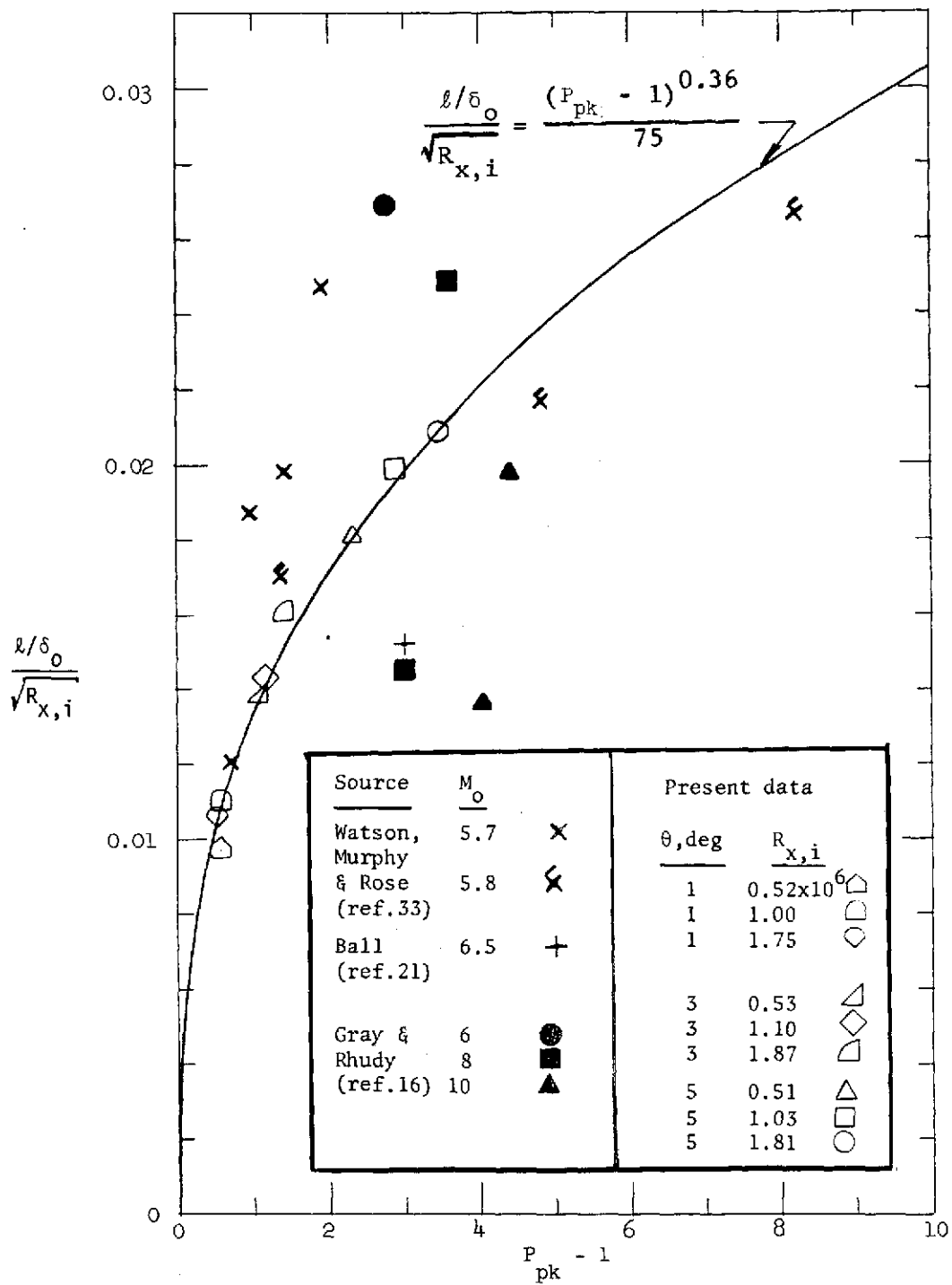Figure 17.- Length of pressure rise upstream of incident shock location.

Figure 18.- Correlation of nondimensional upstream extent of laminar pressure rise with strength of pressure rise.
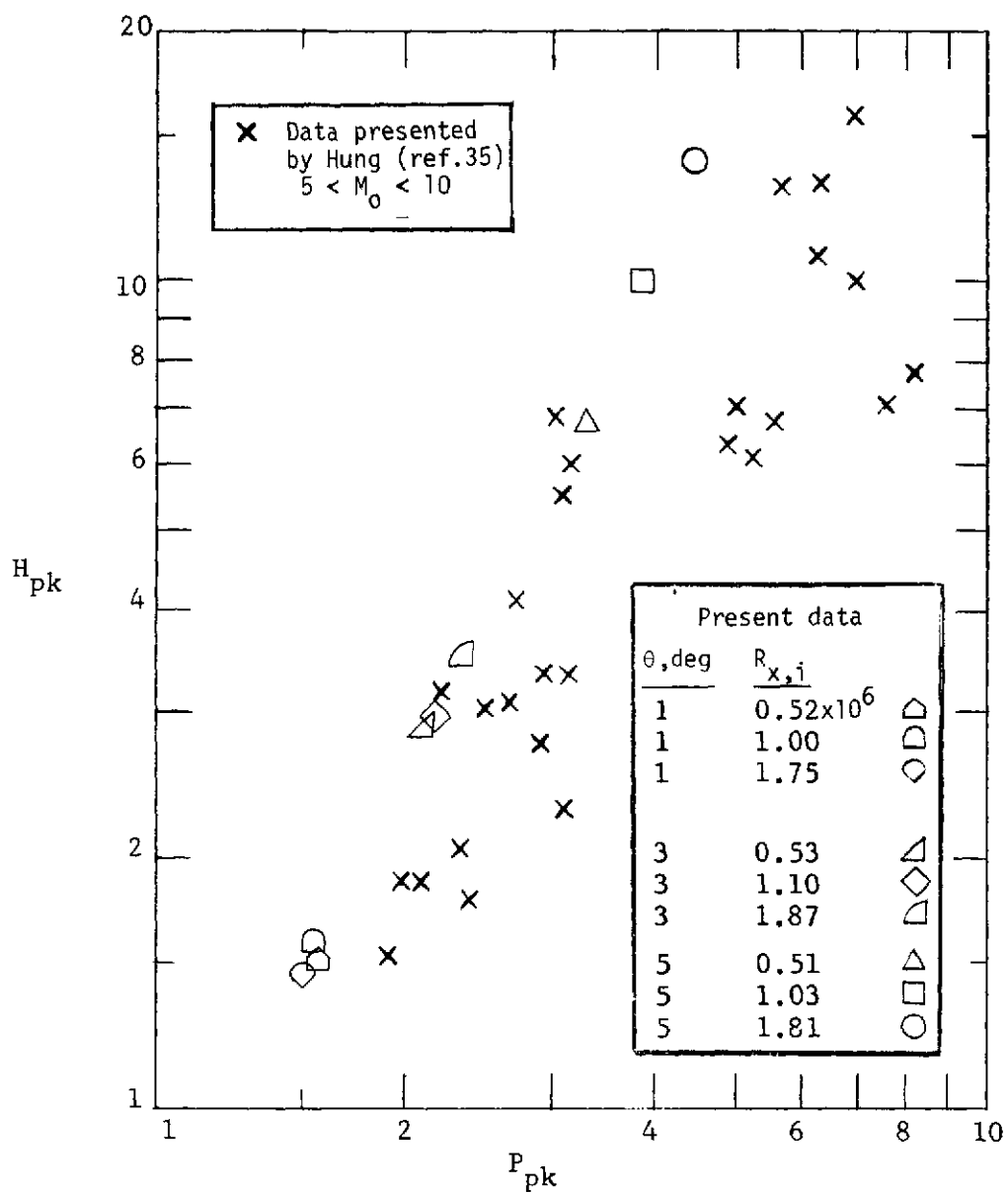
Figure 19.- Peak heating rate amplifications as functions of peak pressure rise ratios.

$$\frac{h_{pk}}{\rho_w V_e c_p}$$

5×10^{-3}

4

3

2

1

θ, deg	R/m
△ 1	2.0×10^6
□ 1	3.7
○ 1	6.3
▲ 3	2.0
■ 3	4.0
● 3	6.6
⬦ 5	1.9
◰ 5	3.7
◐ 5	6.4

Keyes and
Morris (ref. 10)

2×10^4 5×10^4 10^5 2×10^5

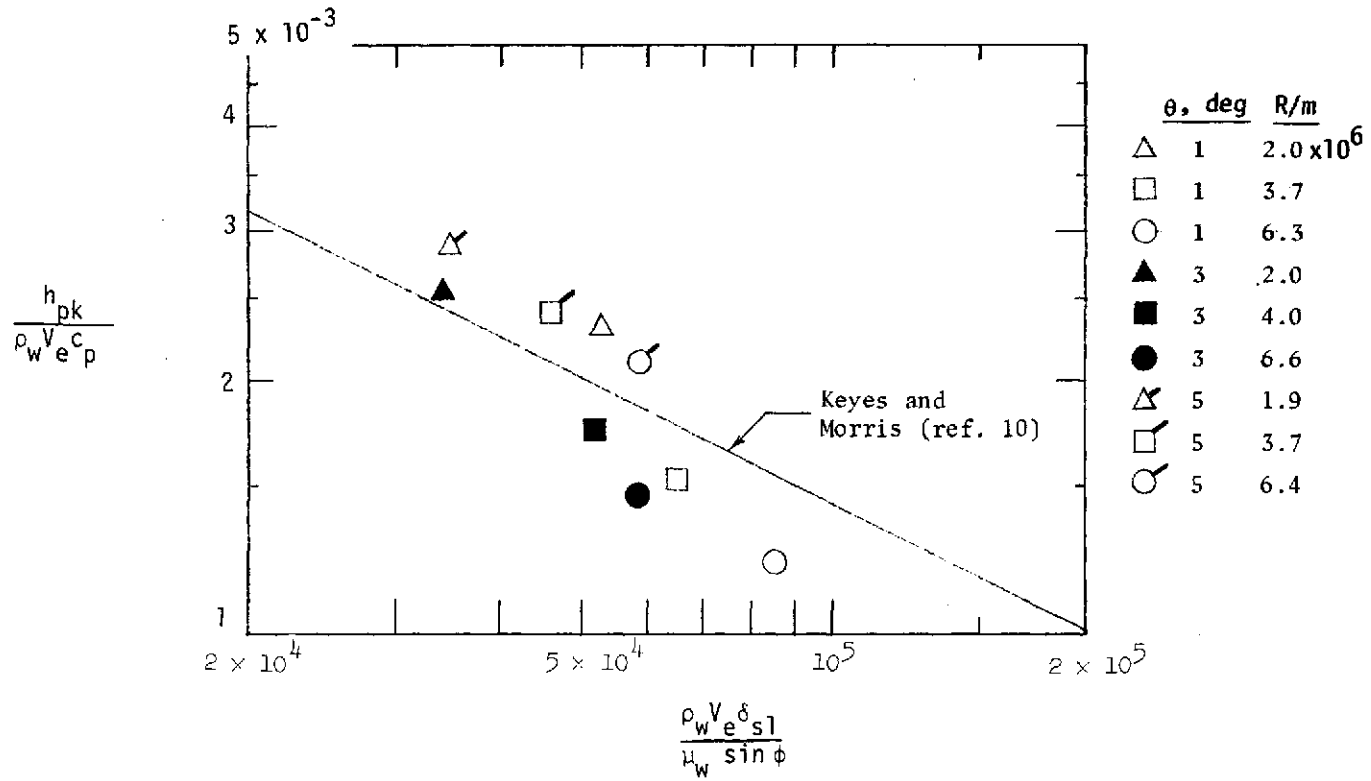$$\frac{\rho_w V_e \delta_{s1}}{\mu_w \sin \phi}$$

Figure 20.- Correlation of peak heating using parameters suggested by
Bushnell and Weinstein (ref. 5).   (See eq. (11).)